LBL-29127
UC-403

Lawrence Berkeley Laboratory
UNIVERSITY OF CALIFORNIA

EARTH SCIENCES DIVISION

Further Modeling Studies of Gas Movement and Moisture Migration at Yucca Mountain, Nevada

Y.W. Tsang and K. Pruess

May 1990

Prepared for the U.S. Department of Energy under Contract Number DE-AC03-76SF00098.

LOAN COPY
Circulates
for 2 weeks
Bldg. 50 Library.
Copy 2
LBL-29127

DISCLAIMER

This document was prepared as an account of work sponsored by the United States Government. Neither the United States Government nor any agency thereof, nor The Regents of the University of California, nor any of their employees, makes any warranty, express or implied, or assumes any legal liability or responsibility for the accuracy, completeness, or usefulness of any information, apparatus, product, or process disclosed, or represents that its use would not infringe privately owned rights. Reference herein to any specific commercial products process, or service by its trade name, trademark, manufacturer, or otherwise, does not necessarily constitute or imply its endorsement, recommendation, or favoring by the United States Government or any agency thereof, or The Regents of the University of California. The views and opinions of authors expressed herein do not necessarily state or reflect those of the United States Government or any agency thereof or The Regents of the University of California and shall not be used for advertising or product endorsement purposes.

Available to DOE and DOE Contractors from the
Office of Scientific and Technical Information
P.O. Box 62, Oak Ridge, TN 37831
Prices available from (615) 576-8401, FTS 626-8401

Available to the public from
National Technical Information Service
U.S. Department of Commerce
5285 Port Royal Road, Springfield, VA 22161
Price: Printed Copy A04, Microfiche A01

Lawrence Berkeley Laboratory is an equal opportunity employer.

LBL-29127

Further Modeling Studies of Gas Movement and Moisture Migration at Yucca Mountain, Nevada

Y. W. Tsang and K. Pruess

Earth Sciences Division
Lawrence Berkeley Laboratory
University of California
Berkeley, California 94720

May 1990

This work was carried out under U.S. Department of Energy Contract No. DE-AC03-76SF00098, administered by the DOE Nevada Office, in cooperation with the Sandia National Laboratories, Albuquerque, New Mexico.

Further Modeling Studies of Gas Movement and Moisture Migration at Yucca Mountain, Nevada

Y. W. Tsang and K. Pruess

Earth Sciences Division
Lawrence Berkeley Laboratory
Berkeley, California 94720

ABSTRACT

In this report we present modeling studies on moisture redistribution processes that are mediated by gas-phase flow and diffusion. Knowledge of the physical processes and parameter sensitivity studies show that moisture removal from Yucca Mountain arising from a lowered humidity of the soil gas at the land surface is controlled by vapor diffusion. With a typical enhanced vapor diffusion strength of β=1, a moisture flux equivalent to $\simeq$ .04 mm/yr of water has been obtained for a range of characteristic curves employed. Both the presence of realistic stratigraphy of alternate layers of nonwelded and welded units, and the choice of characteristics curves, have only minor effects on the magnitude of moisture removal, though characteristic curves play a dominant role in defining the equilibrium liquid-saturation profiles of the layered formation. We are therefore able to conclude from our calculations that the rate of moisture removal from vapor transport has an upper limit of about 0.1 mm/yr. Our calculations for stratigraphic columns with alternate layers of nonwelded and welded units show that order-of-magnitude discontinuities in absolute and relative permeabilities at a lithologic contact give rise to artificially large resistance to flow if the usual numerical scheme of harmonic weighting of absolute permeability and upstream weighting of relative permeability is used. We have resolved the numerical difficulty by invoking a physics-based intuitive model of a "fuzzy lithologic contact", and employing a complete 100% upstream weighting of the effective permeability at all interfaces.

Table of Contents

List of Figures vii

List of Tables ix

Nomenclature x

1. Introduction 1

2. Effect of a Relative Humidity Boundary Condition on Moisture Migration 2

3. Binary Diffusion Strength - Controlling Factor for Amount of Moisture Removal 5

4. Simulation Results for a Medium with Uniform Hydrological Properties 6

5. Inclusion of Stratigraphy in 1-D Column Simulations 9

   5.1 Hydrological Properties 9

   5.2 Reference Case for Layered Medium 11

6. Treatment of a Stratigraphic Interface in Numerical Simulations 12

   6.1 Single-Phase Flow 12

   6.2 Two-Phase Flow 13

   6.3 Effective Continua 15

   6.4 Interpretation of Anomalous Fluxes and Pressure gradients 16

   6.5 Does Explicit Fracture-Matrix Treatment Cure the Problems? 17

   6.6 Upstream Weighting Scheme for Composite Medium 19

7. Simulations with Humidity Boundary Conditions for Stratified Column 20

8. Summary 22

9. Acknowledgments 23

10. References 24

Appendix A

Tables

Figures

List of Figures

Figure 1. One-dimensional vertical column for simulation studies of humidity effects at the land surface.

Figure 2. Fluxes in a column of welded tuff with vapor and air diffusion strength $\beta = .0018$.

Figure 3. Fluxes in a column of welded tuff with vapor diffusion strength $\beta = 1$, and air diffusion strength $\beta = .0018$.

Figure 4. Fluxes at land surface as a function of vapor diffusion strength.

Figure 5a. Division of hydrologic units and spatial discretization for numerical simulation for a layered column of welded and nonwelded tuff.

Figure 5b. Liquid saturation profile in a layered column where the characteristic curves of sample #1 PTN GU3-7 are used for the nonwelded units.

Figure 6. Characteristic curves: (a) Capillary suction, (b) Relative permeability for samples from different hydrologic units.

Figure 7a. Temperature profile of a layered column.

Figure 7b. Vapor pressure profile of the layered column.

Figure 8. Fluxes for reference case of the layered column.

Figure 9. Gas pressure profile of the layered column.

Figure 10. Schematic of a composite medium. Hydrologic parameters change discontinuously at the interface. Spatial discretization for numerical simulation of flow is also shown.

Figure 11. Typical permeability conditions for upward gas flow at a contact between a nonwelded zone (below) and a welded zone (above).

Figure 12. (a) Fluxes and (b) Gas pressure profile of a layered column with the characteristic curves of GU3-7 for the nonwelded units. At the welded and nonwelded interface matrix and fracture flow are handled explicitly.

Figure 13. Liquid saturation profile of a layered column with the characteristic curves of GU3-7 for the nonwelded units. At the welded and nonwelded interface matrix and fracture flow are handled explicitly.

Figure 14. Capillary suction pressure for a layered column using (a) effective continuum (b) explicit matrix-fracture description for the fractured medium at the interface.

Figure 15. Schematic interface of a composite medium to illustrate total upstream weighting of effective permeability.

Figure 16. (a) Fluxes and (b) Gas pressure profile of a layered column with the characteristic curves of GU3-7 for the nonwelded units. At the welded and nonwelded interface multiphase flows are handled by total upstream weighting of effective permeability.

Figure 17. Pressure variation for single-phase steady-state flow with harmonic and total upstream weighting schemes for permeability.

Figure 18. Weighting procedures for absolute (k) and relative permeability (k_r) at interfaces between grid blocks for different classes of flow problems.

Figure 19. (a) Liquid and vapor fluxes and (b) Liquid saturation profile for a layered column with 50% humidity boundary condition imposed (characteristic curves of sample #1 PTN GU3-7 for nonwelded units).

Figures 20. (a) Fluxes and (b) Liquid saturation profile for a layered column in the "reference case" (characteristic curves of Calico Hill sample #5 GU3-15 for the nonwelded units).

Figures 21. (a) Fluxes and (b) Liquid saturation profile for a layered column with 50% humidity boundary condition imposed (characteristic curves of Calico Hill sample #5 GU3-15 for the nonwelded units).

Figure 22. Schematic diagram for explicit matrix and fracture description of the fractured medium at its interface with a porous medium.

List of Tables:

Table 1. Material properties of welded and nonwelded tuff units.

Table 2. Van Genuchten's Parameters for the characteristic curves of different samples in the nonwelded and welded matrix.

Nomenclature

D_{va}	diffusion coefficient for vapor-air mixture, m^2s^{-1}
D^o_{va}	diffusion coefficient at standard conditions STP, m^2s^{-1}
$D_{n,n+1}$	distance between nodal points n and n+1, m
$D_{n,i}$	distance from nodal point n to interface i, m
$D_{i,n+1}$	distance from interface to nodal point n+1, m
$\mathbf{F}_l$	liquid mass flux, $kg/m^2.s$
$\mathbf{g}$	acceleration of gravity, m/s^2
h	humidity, dimensionless
K	thermal conductivity, Joule-m/K
k	absolute permeability, m^2
k_f	absolute fracture permeability, m^2
k_m	absolute matrix permeability, m^2
$\bar{k}$	absolute (continuum) permeability, m^2
$\bar{k}_f$	absolute (continuum) fracture permeability, m^2
$\bar{k}_m$	absolute (continuum) matrix permeability, m^2
k_r	relative permeability, dimensionless
$k_{f,\beta}$	relative permeability in fracture for phase β
$k_{m,\beta}$	relative permeability in matrix for phase β
k_β	effective continuum relative permeability normalized to total continuum permeability, $\bar{k}_m + \bar{k}_f$
k_i	absolute interface permeability w.r.t. total continuum permeability, m^2
$\hat{k}_\beta$	effective continuum relative permeabiity normalized to matrix continuum permeability, $\bar{k}_m$
$\hat{k}_i$	absolute interface permeability w.r.t. matrix continuum permeability, m^2
k_{eff}	effective permeability $k \,.\, k_r$, m^2
$k_{\beta,eff}$	effective permeability to phase β, m^2
ln	natural logarithm, dimensionless
n	Van Genuchten parameter for characteristic curves, dimensionless

P	pressure, Pa
P_{cap}	capillary pressure, Pa
P_o	Standard pressure, 1 bar = 10^5 Pa
R	gas constant for water vapor, 461.5 J (kg K)$^{-1}$
S_{EF}	effective liquid saturation, dimensionless
S_l	liquid saturation, dimensionless
S_r	residual saturation, dimensionless
T	temperature, degrees Kelvin
T_o	standard temperature, 273.15K

GREEK

α	Van Genuchten parameter for characteristic curves, m^{-1}
β	strength of vapor diffusion in a porous medium, dimensionless
χ_g^κ	mass fraction of the κ^{th}component in the gas phase, dimensionless
λ	Van Genuchten parameter for characteristic curves
μ	viscosity, Pa s
ϕ	porosity, dimensionless
ρ	density, kg/m^3
τ	tortuosity factor in diffusion coefficient, dimensionless
θ	parameter in diffusion ceofficient, dimensionless

SUBSCRIPTS

a	medium a
b	medium b
β	phase, gas or liquid
f	fracture
g	gas phase
i	interface
l	liquid phase
m	matrix
n	index of discretization nodes
n+1	index of discretization nodes

1. Introduction

The present report is a summary of our studies in 1989-1990 to examine the effect of atmospheric boundary conditions at the land surface on the ambient gas and moisture movements at Yucca Mountain. These studies are a continuation of the preliminary investigations which we have reported previously (Tsang and Pruess, 1989). Our interest in the gas phase flow at Yucca Mountain arises primarily from the concern that a few radionuclides, such as C^{14}, could be transmitted through gaseous pathways (Von Konynenburg et al., 1985, 1986; Ross, 1987). An understanding of gas phase flow effects is necessary for determining the quantity of gaseous radionuclides that could be released at the surface. Gas phase flow has other ramifications besides providing potential pathways for radionuclides to the accessible environment. Through vaporization and condensation processes coupled with vapor transport, gas phase flow effects may indirectly influence the distribution of moisture and liquid phase flow throughout the unsaturated zone.

It is clear that factors such as barometric pressure, temperature, relative humidity of atmospheric air, precipitation, wind velocity, topography, etc., may all play a role in the coupled gas and liquid flow at Yucca Mountain. The effects of topography and seasonal temperature variation on gas flow at Yucca Mountain have been studied by Weeks (1987) and Kipp (1987). Two wells located at the crest of Yucca Mountain that tap highly fractured welded tuffs were observed to show substantial air exchange with the atmosphere (Weeks, 1987). During winter, the wells exhaust air almost continuously at relatively high velocity, typically about 3 $m\,s^{-1}$. This air flow is attributed to the topographic effect: the column of atmospheric air extending from a fractured-rock outcrop on the hillside to the hillcrest will be colder, drier, and hence denser during cold weather than the column of soil gas extending from the hillside outcrop through the highly permeable fractured rock and the well to the same hillcrest altitude. Thus, during winter, air will enter the outcrop and migrate through the fractured rock to exhaust out the well.

To examine the hypothesis that the seasonal variation of air temperature at the mountain surface, coupled with the topographic relief, may cause a natural, annually periodic air circulation through the unsaturated zone, a numerical simulation was carried out by Kipp (1987). The simulated region was taken to be a vertical slice of

rectangular shape, 150 m high and 500 m wide part way through the mountain. The mountain side extends down to 100 m below the mountain crest. The simulation results show that the temperature field is affected by the seasonal variations only within 20 m of the land surface. The velocity fields show that summer is the only season with a general flow pattern in from the mountain crest, down and out the mountain side. The other three seasons show flow entering the mountain side, rising and exiting at the mountain crest. Kipp estimated a net water-vapor transport out from the simulated region of the mountain equivalent to 0.042 mm yr^{-1} of net infiltration.

In a previous report (Tsang and Pruess, 1989) in which we discussed the results of our preliminary investigation of gas flow effects and moisture migration at Yucca Mountain, we showed that the vapor fluxes as a result of barometric pumping and of a reduced humidity boundary condition at the land surface will be on the same order of magnitude as those for seasonal temperature variation and topography in Kipp's simulation. Hence, although the upward moisture fluxes from different topographic and atmospheric boundary effects are all small, they are not insignificant because they are on the same order of magnitude as the supposed liquid infiltration of less than 0.4 mm/yr at Yucca Mountain (Montazer and Wilson, 1984), and may lead to the potential overall drying of the mountain. In view of the role these processes driven by land surface boundary conditions may play in affecting the moisture content of the mountain, we have continued our preliminary investigation in the direction of a parameter sensitivity study. Moreover, since our preliminary study (Tsang and Pruess, 1989) was based on the simplifying assumption that the formation was composed only of the welded Topopah Spring Tuff characteristic of the repository horizon, it seems natural that the effect of stratigraphy needs to be considered in the investigation of moisture flux movements driven by boundary conditions. Results obtained from incorporating stratigraphy, and from parameter sensitivity studies, will be the focus of this report.

2. Effect of a Relative Humidity Boundary Condition on Moisture Migration

At the land surface, humid formation gas contacts much drier atmospheric air. Near this contact, the humidity of the soil gas may be considerably lower than at greater depth, where we expect equilibrium with the liquid phase and close to 100% humidity. The lower relative humidity of the soil gas may be imposed as a boundary condition at the land surface, providing a driving force for the upward movement of moisture in the form of vapor (as well as liquid because of the vapor pressure lowering

effect as discussed below). Our earlier calculations on a column of welded tuff (Tsang and Pruess, 1989) gave estimates on the order of .001 mm/yr and .0002 mm/yr for the liquid and vapor flux, respectively, from an imposed boundary condition of 50% relative humidity. Subsequently, it has come to our attention (Ross, 1984) that vapor diffusion in partially saturated media can be strongly enhanced by phase change effects. This phenomenon is rather well documented in the soil literature (e.g. Philip and de Vries, 1957, Cary and Taylor, 1962 a, b; Hanks et al., 1967; Weeks et al., 1968; Jury and Letey, 1979). Since the strength of the binary diffusion in the formation plays the key role in affecting vapor transport, we have reexamined the effect of the lowered relative humidity boundary condition on moisture fluxes, paying particular attention to their dependence on the strength of binary diffusion in the soil gas.

Before presenting the results, we shall outline the formulation of the problem, which has been presented in our previous report, but is included here again in order to make this report somewhat self-contained.

In the presence of capillary suction vapor pressure is reduced from its saturated value according to Kelvin's equation (Edlefsen and Anderson, 1943):

$$P_v(T,S_l) = P_{sat}(T)\exp\left[\frac{P_{cap}(S_l)}{\rho_l R T}\right] \tag{1}$$

where ρ_l is the density of water, T is absolute temperature, and R is the gas constant for water vapor, $8.314\,\mathrm{J}/18.016\times10^{-3}\,\mathrm{kg\,K} = 461.5\ \mathrm{J\ (kg\,K)^{-1}}$. Equation (1) denotes the vapor pressure lowering effect. If capillary effects provide for the presence of soil moisture all the way up to the ground surface, a reduced humidity level can come about due to vapor pressure lowering. The relative humidity is defined as $h = P_v/P_{sat}$, so that

$$h = \frac{P_v}{P_{sat}(T)} = \exp\left[\frac{P_{cap}(S_l)}{\rho_l R T}\right]. \tag{2}$$

At Yucca Mountain it appears that because of the very small pore sizes of the tuffs, the capillary effects are strong, and so the capillary fringe extends all the way to the ground surface. The reduced humidity level near the ground surface gives rise to an equivalent capillary suction expressed according to the relation

$$P_{cap}(S_l) = (\ln h)\,\rho_l RT. \tag{3}$$

The equivalent suction pressure may be quite strong even with moderate lowering of

the humidity level. The strong suction pressure provides a driving force for an upward movement of liquid water toward the low humidity boundary, given by

$$\mathbf{F}_l = -\bar{k}\,\frac{k_{rl}}{\mu_l}\rho_l\,(\nabla\,(P_g+P_{cap})-\rho_l\,\mathbf{g}), \tag{4}$$

where $\bar{k}$ is the saturated permeability of the fractured porous medium, k_{rl} is the relative permeability to the liquid phase at the liquid saturation S_l, μ_l is the viscosity of the liquid, P_g is the gas pressure, $\mathbf{g}$ is the gravitational acceleration, and $\mathbf{F}_l$ is the liquid mass flux.

The lowered-humidity boundary condition implies a composition gradient in the gas phase, giving rise to a downward diffusive flux of air and an upward flux of vapor. The binary diffusion gas flux is described by

$$\mathbf{F}^{\kappa} = -D_{va}\,\rho_g\,\nabla\chi_g^{\kappa}, \tag{5}$$

where κ is the component index for the gas phase (κ=air or vapor), χ_g^{κ} is the mass fraction of the κth component in the gas phase, and D_{va} is the diffusion coefficient for the vapor-air mixture in a porous medium, given by (Vargaftik, 1975; Walker et al., 1981)

$$D_{va} = \tau\phi S_g D_{va}^{o}\,\frac{P_o}{P}\left[\frac{T}{T_o}\right]^{\theta} \tag{6}$$

Here, ϕ is the porosity, S_g is the gas saturation, τ is a tortuosity factor, which is dependent on the pore geometry, and T is the temperature in degrees Kelvin. In our previous report (Tsang and Pruess, 1989), we used the values of D_{va}^{o} = 2.14 times $10^{-5}\,m^2\,s^{-1}$ at standard conditions of $P_o = 1$ bar and T_o = 273.15 K and θ = 2.334 (Langkopf, 1987; Bird et al., 1960).

The parameter group $\beta = \tau\phi S_g$ specifies properties relevant to binary diffusion in a porous medium. For a column of welded tuff in which the matrix pores are partially saturated, the fractures are believed to be nearly drained, i.e. $S_g \approx 1$. In the previous report, we used values specific to the fractures in the welded tuff for β, namely: $\tau = 1$, $S_g = 1$ and $\phi_f = .0018$, giving rise to a value of β = .0018. For the rock matrix, typical values such as $\tau \approx .2$ (Langkopf, 1987), $S_g \approx .2$ and $\phi_m = .11$ result in a slightly larger value of β in the range of .004.

3. Binary Diffusion Strength - Controlling factor for Amount of Moisture Removal

In the soil science literature, there is much experimental evidence that β for water vapor is typically in the range of 1 to 3.5 for a variety of porous media (e.g. Cary and Taylor, 1962a,b; Hanks et al., 1967; Weeks et al., 1968). These measurements indicate that the simple mechanism of gas-phase diffusion of water vapor modified for effects of pore geometry grossly underestimates the amount of vapor transported within the porous medium. In an estimation of condensation fluxes from vapor in deep unsaturated zones, Ross (1984) has used a value of $\beta = 2$. Philip and deVries (1957) suggested two enhancement mechanisms to account for the discrepancy between theory and experiment. The first mechanism postulated was that the temperature gradients present within air-filled pores are higher than the overall macroscopic gradient of the porous medium because the thermal conductivity of the water vapor is significantly lower than the thermal conductivity of the liquid and solid phases of the composite porous medium. The second enhancement mechanism is the condensation and re-evaporation of water vapor at liquid "islands", which could result in the vapor phase effectively utilizing some of the liquid filled pore space as part of the transfer path (Verma, 1986). Jury and Letty (1979) modified the theory of Philip and deVries and showed that not only do the liquid islands give rise to the replacement of the liquid-filled pore space by vapor-filled pore space, but that the liquid gap in effect also shortens the vapor path, giving rise to further enhancement in the pore geometry factor β. Their theoretical calculation shows that β is essentially independent of water content over a large range of liquid saturations, with a value on the order of one. This is consistent with the experimental studies whose results Jury and Letty also summarized. The enhanced value of $\beta \approx 1$ for vapor diffusion is orders of magnitude larger (typically by factors from 250-500 in our case) than that of the parameter group $\tau\phi S_g$ in Equation 6 derived from material properties appropriate for air diffusion, implying that the vapor diffusion and the air diffusion no longer have identical magnitudes.

It is clear from the above that the enhancement of vapor diffusion from pore-level phase change processes is large, so that a revision of our calculations with humidity boundary conditions as presented in our 1989 report is warranted. We have therefore performed a sensitivity study employing different enhanced values of β for vapor diffusion, while retaining values of $\tau\phi S_g$ used previously for air diffusion. In all other aspects, such as simulation procedures and problem specification, our numerical

simulations are identical to those described in our previous report. We shall briefly review the method of simulation here; for specific details we refer the reader to the earlier report (Tsang and Pruess, 1989). Calculations were carried out by means of an in-house version of the numerical simulator "TOUGH" (Transport Of Unsaturated Goundwater and Heat; Pruess, 1987), which includes vapor pressure lowering effects. To focus on the vertical movement of fluxes, the simulation was carried out in one dimension, in a vertical tuff column of 600 m, which is the approximate distance of the land surface to the water table at the proposed repository site (Figure 1). We first employed a highly simplified stratigraphic description, assuming uniform hydrologic parameters that were representative of the proposed repository host formation (the Topopah Spring welded unit). The formation parameters are those given in Tables 1 and 2 for the welded unit. The numerical computation is first carried out without the imposition of a lowered humidity boundary condition, hereafter refered to as the "reference case". The ground surface and the water table serve as constant temperature boundaries maintained at 286 K and 304 K, respectively. The water table serves also as a pressure boundary with the constant pressure P_o of 1 bar, while a "no flow" boundary is imposed at the top, so that the gas pressure at each elevation will adjust itself to $P_o - \rho gz$, whereas the equilibrium liquid pressure depends also on the capillary suction. The simulation provides, as function of elevation, the equilibrium profiles of temperature, gas pressure, vapor pressure and liquid and gas saturation before the boundary condition of lowered-humidity at the land surface is engaged. Then we implement the lowered-humidity boundary condition by imposing, at the land surface, an additional liquid suction pressure corresponding to Equation 2.

4. Simulation Results for a Medium with Uniform Hydrological Properties

Fluxes in the liquid and gas phase are shown in Figures 2 and 3. Results obtained prior to imposition of reduced-humidity boundary conditions are labeled "reference case", and those with imposed humidity boundary condition are labeled accordingly by "50% humidity". We should add here that since the capillary suction is non-zero at the top of the column in the "reference case", the humidity at the top of the column, as defined in Equation 2 for the "reference case", is not exactly 100%, but is about 97%. Units of flux are in both kg/m^2-s (bottom scale) and mm/yr of water (top scale). The label "vapor" in the figures denotes the total vapor flux arising from binary diffusion, as represented by Equation 5, as well as pressure-driven Darcy flow. The figures

display the fluxes as a function of elevation, with positive values for upward fluxes, and negative values for downward fluxes. Figure 2 shows the results with $\beta = \tau\phi S_g$ = .0018 for both vapor and air diffusion, the choice in our previous report (note the different scales for Figure 2a and 2b). Figure 3 shows the result with the enhanced value of β=1 for vapor diffusion, and the original value, $\tau\phi S_g$ = .0018 for the air diffusion. Results for the reference case are qualitatively similar in Figures 2a and 3a, though the fluxes are several orders of magnitude larger in Figure 3a because of the enhanced value of β for vapor diffusion (Equations 5 and 6 show that the binary diffusion fluxes should scale as β). For the "reference case", the upward vapor flux is balanced by the downward flow of the condensed liquid, resulting in zero net moisture migration. The larger magnitude of the vapor fluxes at depth arises from the geothermal gradient. With the imposition of a 50% relative humidity boundary condition, both the liquid flux and the vapor flux are upward, giving rise to the net upward migration of moisture. For β=.0018 in Figure 2b, the upward moisture flux consists mainly of the liquid phase at depth, and only switches to predominantly vapor within 25 m of the land surface. However, for the case where β=1, Figure 3b shows that the upward moisture flux is predominantly vapor. Vapor diffusion is driven by ∇P_v, which is essentially fixed by ∇T. Hence, vapor flux first decreases with elevation from the water table because of the decrease of temperature; at 300 m above the water table, vapor pressure lowering effects come into play from the lowered humidity boundary condition applied at the land surface, and the magnitude of vapor flux increases with elevation. The moisture flux from the upper portion of the formation consists almost entirely of vapor. The decrease of liquid flux with elevation arises from non-linear liquid-flow effects, since the lower liquid saturation with elevation from the imposed boundary condition, while giving rise to a stronger upward capillary driving force, also results in a rapid decrease in liquid relative permeability. The total upward moisture flux is seen to be $\approx$ 0.0015 mm yr^{-1} in Figure 2b and $\approx$ .04 mm yr^{-1} in Figure 3b.

In addition to the two values of β of Figures 2 and 3, simulations were also carried out for two intermediate values of β=.05, and .33. The simulated results are summarized in Figure 4, which is a log-log plot of fluxes versus the geometric factor β. The upward vapor fluxes plotted are the simulated values at 2.5 m below the land surface. We note that when no lowered humidity boundary condition is present, the vapor fluxes fall on a straight line of unit slope on the log-log plot, illustrating the linear dependence of the diffusion vapor flux on β, which follows from Equations 5

and 6. With the 80 % humidity boundary condition at the land surface, the upward moisture flux is predominantly carried by the vapor phase when β is larger than .05. Only for the smallest value of β=.0018 does the liquid phase flux contribute significantly to the total upward moisture flux. For the range of values of β examined, the rate of moisture removal ranges from about .002 mm/yr to .04 mm/yr with the lowered humidity boundary condition of 80%. Similar results were obtained for the humidity boundary condition of 50%. Figure 4 therefore summarizes the following: (1) For the reference case, the vapor flux increases linearly with the geometric factor β, which measures the strength of the vapor diffusion process. In the absence of an imposed lowered humidity boundary condition, the upward vapor flux is balanced by the downward condensed liquid flux, resulting in no net loss of moisture from the formation. (2) With the lowered-humidity boundary condition at the surface, the magnitude of the total moisture flux is larger than, but of the same order of magnitude as, the vapor flux of the reference case. Hence the strength of the vapor diffusion both controls, and gives a good estimate, of the amount of moisture which is removed from the formation under an imposed lowered relative humidity boundary condition.

It is significant that β is shown to control the amount of moisture removed from the formation. By varying β over a large range up to the greatly enhanced value of 1, we believe we have bracketed the possible range of magnitude of moisture flux out of a column of welded tuff. We expect our estimates to remain relevant even in the presence of alternating layers of welded and nonwelded tuff. The different material properties and characteristic curves of the welded and nonwelded tuff may strongly affect properties such as equilibrium liquid saturation, yet the range of β studied should continue to dictate the rate of vapor-dominated moisture removal from humidity boundary conditions. To substantiate our claim that results as shown in Figure 4 for a column of welded tuff are pertinent to the actual system with realistic stratigraphy, we now turn to sample calculations where the effects of stratigraphy are included.

5. Inclusion of Stratigraphy in 1-D Column Simulations

5.1. Hydrologic Properties

Based on an east-west cross section at Yucca Mountain (for example, Peters and Klavetter, 1988, Figure 1) we estimate the average thickness for the respective hydrologic units above the water table to be 125 m for Calico Hill nonwelded tuff, 325 m for Topopah Spring welded tuff, 50 m for Paintbrush nonwelded tuff and 100 m for Tiva Canyon welded tuff. The division of the hydrologic units is shown in Figure 5a, which also shows the grid used in the numerical simulations. The smallest grid blocks adjacent to a welded- nonwelded interface are 5 m thick.

After a review of the material properties (physical, thermal, hydrological) of the different units as given in the NNWSI Reference Information Base (version 2.002, 1987), we feel that it is a good approximation to assign one set of properties to the nonwelded units (NW) (Paintbrush Canyon and Calico Hill vitric) and another set of properties to the welded (W) units (Topopah Spring 1, 2, and 3 and Tiva Canyon). Table 1 summarizes the material properties used in our calculations. The material properties in Table 1 for the welded units (applicable to both the Tiva Canyon and the Topopah Spring) differ only very slightly in certain entries (rock grain density, dry formation heat conductivity, and matrix porosity) from those used in our earlier report (Table 2 in Tsang and Pruess, 1989), where properties specific to the repository horizon in the Topopah Spring were tabulated. The welded tuff units are intensely fractured, with an average (continuum) fracture permeability about four orders of magnitude larger than the matrix permeability (Peters and Klavetter, 1988). On the other hand, the nonwelded units are sparsely fractured and are characterized by merely the matrix permeability, which is of the same order of magnitude as the continuum fracture permeability in the welded units (Peters and Klavetter, 1988). As for the characteristic curves, Van Genuchten parameters have been fitted to the laboratory measurements of core samples from different hydrologic units (Klavetter and Peters, 1986). The Van Genuchten function expresses the liquid saturation S_l in terms of ψ, the capillary pressure head in m of H_2O,

$$S_l = 1 - S_r \left[\frac{1}{1 + |\alpha\psi|^n} \right]^{\lambda} + S_r \tag{7}$$

where S_r is the residual saturation and α and n are the fitting parameters. The parameter λ is equal to $1-1/n$. The corresponding relative permeability as a function of

pressure head is

$$k_{rl} = \left[1 + |\alpha\psi|^n\right]^{-\lambda/2} \left\{1 - \left[\frac{|\alpha\psi|^n}{1 + |\alpha\psi|^n}\right]^{\lambda}\right\}^2. \tag{8}$$

In TOUGH, the suction pressure and relative permeability are expressed in terms of liquid saturation, with the effective liquid saturation S_{EF} defined by

$$S_{EF} = \frac{S_l - S_r}{1 - S_r}. \tag{9}$$

Converting the suction head ψ in meters of water to capillary pressure, $P_{suc} = \rho g \psi$, we have

$$P_{suc} = \frac{\rho g}{\alpha}\left(S_{EF}^{-1/\lambda} - 1\right)^{1-\lambda} \tag{10}$$

and

$$k_{rl} = \sqrt{S_{EF}}\left(1 - \left[1 - S_{EF}^{1/\lambda}\right]^{\lambda}\right)^2 \quad . \tag{11}$$

The Van Genuchten fitting parameters have been tabulated by Klavetter and Peters (1986), and are reproduced here in Table 2, where the samples are numbered from #1 through #6. In Figure 6 we have plotted the characteristic curves as a function of liquid saturation using the parameters for the different samples from the different units. For the welded units, we use the same characteristic curves as in our previous report, where the fractured porous medium was treated as an effective continuum (Pruess et al., 1985; 1988; and Appendix A of Tsang and Pruess, 1989). The matrix parameters correspond to core sample #3 TSW G4-6 for the welded Topopah Spring unit, and the relative permeability in the fracture is assumed to be a linear function of saturation. For the nonwelded units, we note that the characteristic curves of the samples #1 PTN GU3-7 from Paintbrush Canyon and sample #4 CHNV GU3-14 from Calico Hills are rather similar, justifying our approximation to assign one set of properties to both nonwelded units. The very flat slope of the suction curve for these two samples, over a large range of liquid saturation, indicates a rather narrowly peaked pore size distribution for the nonwelded tuff. On the other hand, the shape of the suction curves for the samples #2 PTN GU4-2 from the Paintbrush Canyon and #5 CHNV GU3-15 from the Calico Hills suggest a broader pore-size distribution. The different characteristic curves would mainly affect the equilibrium liquid saturation profile of the stratified formation. Wang and Narasimhan (1988) have found that the characteristics curves of #2

GU4-2 and #5 GU3-15 give higher liquid saturations in the non-welded units which are in better agreement with the ambient liquid saturation in the Paintbrush Canyon unit than if the characteristic curves of #1 were used. We have carried out sets of simulations employing different curves for the nonwelded units: One with the characteristic curves of #1 PTN GU3-7 assigned to both the Paintbrush Canyon and Calico Hills nonwelded units, and the other with the characteristic curves of #5 CHNV GU3-15 assigned to the nonwelded units.

5.2. Reference Case for Layered Medium

To simulate a hypothetical "natural state" with zero net infiltration prior to imposition of lowered humidity boundary conditions, we employ the same boundary conditions as specified in the "reference case" discussed in section 3 (see Figure 1). The strength of the vapor diffusion β_v is kept equal to the enhanced value of 1 for the entire column of alternating layers of welded and nonwelded tuff. The strength of the air diffusion is $\beta_a = \tau\phi S_g$ and the tortuosity factor τ was chosen to be 0.25, so that β_a is typically of order 0.01. In Figure 5b we show the steady-state liquid saturation profile of the column of alternating layers of welded (characteristics curves of #3 TSW G 4-6) and nonwelded tuff (characteristic curves of #1 PTN GU3-7). Note that the liquid saturation in the nonwelded units is slightly above 0.1, whereas the saturation in the welded units is much higher, on the order of 0.8. The different equilibrium liquid saturations arise from the different capillary suction curves of the nonwelded and welded units. In Figure 6a, the capillary suction at 80% saturation of the welded sample #3 TSW G 4-6 is shown to equal the suction in the nonwelded sample #1 PTN GU3-7 at 10% saturation. In Figure 7a we show the temperature profile of the 1-D layered column. Note the slight change of linear slope in the alternate layers as a result of the different thermal conductivities specified for the welded and nonwelded units. The temperature profile (Figure 7a) gives rise to an increase in vapor pressure with depth (Figure 7b), which drives an upward vapor flux by diffusion. Smaller effects on vapor pressure occur from vapor pressure lowering.

The fluxes for the reference case are shown in Figure 8. For the time being, ignore the anomalies (sharp dips) at the interfaces of the nonwelded and welded layers at elevation 450 m. We shall discuss these flux anomalies below. Apart from these anomalies, we note that the same physical processes are active here as for the uniform column of welded tuff. The excess vapor from the upward diffusion flux condenses at

the lower temperatures encountered at higher elevations. At equilibrium, the upward vapor flux is balanced by the downward condensation liquid flux, resulting in no net movement of moisture for the reference case. It is clear from Figure 7b that the vapor pressure gradient is larger in the nonwelded units than the welded units, accounting for the larger fluxes in the nonwelded units. The magnitude of the fluxes are comparable with those shown in Figure 3 for the welded column with enhanced vapor diffusion $\beta = 1$. A test case was run where the values of β are reduced by a factor of 10 in both the welded and nonwelded units. As was anticipated (cf. Figure 4), the computed profiles of the vapor and liquid fluxes resemble that of Figure 8, except that their magnitudes are reduced by about a factor of 10.

6. Treatment of a Stratigraphic Interface in Numerical Simulations

The anomalous dip in liquid and vapor fluxes at the lithologic contact between nonwelded and welded units at 450 m elevation (Figure 8) warranted further study. In addition to the dip in fluxes as shown in Figure 8, very large gas pressure-gradients are found at the two other lithologic contacts of nonwelded and welded units at elevations of 125 m and 500 m, as shown in Figure 9. Both the dip in fluxes in Figure 8 and the large gas-pressure gradients in Figure 9 are indicative of particularly large resistance to the fluid flow at the interfaces between nonwelded and welded units. Such flow resistances appear to be spurious and due in some way to approximations made in the spatial discretization of the flow system for numerical simulation. To clarify this issue, let us examine more closely the handling of flow permeability terms at a stratigraphic interface.

6.1. Single-Phase Flow

Consider a contact between two formations (zones) of different porosity, absolute and relative permeability, and capillarity (Figure 10). From a mathematical viewpoint, the interface between the two zones represents a surface of discontinuity, where hydrological and thermal properties of the media change in discontinuous fashion. In contrast, away from the interface all formation parameters vary in a smooth and continuous way (when averaged over suitable spatial domains, i.e., an REV). Numerical simulation of flow across the discontinuity encounters some special problems. For example, what is the proper permeability to use when calculating flow between grid blocks n and n+1 (Figure 10)? For single phase flow, it is well known that the proper

interface permeability k_i is obtained by harmonic weighting,

$$\frac{D_{n,n+1}}{k_i} = \frac{D_{n,i}}{k_a} + \frac{D_{i,n+1}}{k_b} \tag{12a}$$

where $D_{n,n+1} = D_{n,i} + D_{i,n+1}$ is the distance between the nodal points. Solving for k_i, we have

$$k_i = \frac{k_a k_b D_{n,n+1}}{k_a D_{i,n+1} + k_b D_{n,i}}. \tag{12b}$$

Equation (12) can be derived by decomposing the pressure difference between volume elements (grid blocks) n and n+1

$$P_n - P_{n+1} = P_n - P_i + P_i - P_{n+1} \tag{13}$$

where P_i is the pressure at the interface, and then applying Darcy's law separately over the flow paths $n \rightarrow i$ and $i \rightarrow n+1$, with the constraint that flux is conserved across the interface. Indeed,

$$P_n - P_{n+1} = \frac{\mu F}{\rho} \frac{D_{n,n+1}}{k_i} \tag{14}$$

and

$$P_n - P_i = \frac{\mu F}{\rho} \frac{D_{n,i}}{k_a}, \tag{15a}$$

$$P_i - P_{n+1} = \frac{\mu F}{\rho} \frac{D_{i,n+1}}{k_b} \tag{15b}$$

which, when inserted into Equation (13), yields (12a). (Equations 12 hold regardless of the orientation of the interface relative to the vertical.)

6.2. Two-Phase Flow

The problem of interface permeability becomes much more difficult in two-phase flow, because in addition to absolute permeabilities we also must deal with relative permeabilities of the individual phases. The effective permeabilities for a fluid phase β are given by $k_a k_{ra,\beta}$ and $k_b k_{rb,\beta}$, respectively, in zones a and b. Let us approach the problem of interface permeability by considering one-dimensional, steady two-phase flow without phase change. Under these conditions, effective permeability $k k_{r,\beta}$ of a phase β is a time-independent spatial field and, if it is non-zero at some point, must be

non-zero throughout the flow domain. The reasoning that leads to harmonic permeability weighting for single-phase flow is then applicable, and effective interface permeability would be given by the harmonic weighting of effective phase permeabilities,

$$\frac{D_{n,n+1}}{k_i \cdot k_{ri,\beta}} = \frac{D_{n,i}}{k_a \cdot k_{ra,\beta}} + \frac{D_{i,n+1}}{k_b \cdot k_{rb,\beta}}. \tag{16}$$

However, this reasoning and the weighting scheme Equation (16) are not generally applicable to transient flow conditions, or to flow processes involving a change of phase. In either circumstance, sharp phase fronts may develop in which a fluid phase may flow into a region in which its relative permeability is zero. Phase fluxes change in a discontinuous fashion at such fronts. Equation (16) would then yield a vanishing effective interface permeability, which would make it impossible for a fluid phase to enter a region in which it is not already mobile; this clearly is an unphysical outcome. From a mathematical viewpoint, the breakdown of the harmonic weighting scheme Equation (16) is related to the possibility of flux discontinuities in two-phase flow, which are accompanied by advancing phase fronts, or by surfaces on which a change of phase takes place. A discontinuity in flux precludes application of the reasoning that led to Equation (12) or (16).

In transient two-phase flows, or two-phase flows with phase change, it must be possible for the effective interface permeability in a spatially discretized description of flow to be non-zero even when the "down-stream" effective permeability is zero; otherwise, the invading phase would never be able to get across the interface, regardless of the magnitude of driving pressures. Relative permeability must not get overwhelmed by a downstream value of zero, as would occur with the harmonic weighting, Equation (16). What then is the proper interface permeability to use?

Let us first consider media with uniform hydrologic properties throughout. Clearly, absolute permeability at an interface is then equal to the (identical) value in the adjacent grid blocks. As to the relative permeability at the interface, it is well established that the proper choice is the "fully upstream weighted" value: if phase b flows from a –> b, we must take $k_{ri}=k_{ra}$; if flow is from b –> a, we have $k_{ri}=k_{rb}$. Any weighting scheme that involves less than full upstream weighting for relative permeability will lead to an erroneous prediction of the speed at which the invading fluid advances (Aziz and Settari, 1979).

We are not aware of any published work on interface weighting rules for two-phase flow in composite media, in which phase fronts may propagate across permeability discontinuities. In past numerical simulation work, we have generally maintained full upstream weighting of relative permeability, and have used harmonic weighting for absolute permeabilities. This weighting is appropriate for single-phase flow in composite media (with permeability discontinuities), as well as for two-phase flow in media with uniform hydrologic properties. However, the spurious flow resistances at lithologic contacts noted above indicate that new problems arise in two-phase flow in composite media, and a re-thinking of interface weighting procedures is required. Before proceeding with that task, let us consider the additional complications arising for fractured porous media which are approximated as effective continua.

6.3. Effective Continua

When using the effective continuum approximation for flow in fractured porous media, different conventions may be adopted for normalizing the relative permeability functions (Pruess et al., 1990). In a medium with uniform hydrologic properties, these alternative normalizations are completely equivalent. However, a difficulty arises in composite media with discontinuous changes in permeability. For a fractured medium, effective permeability to a fluid phase β can be written as

$$k_{\beta,\,\mathrm{eff}} = \bar{k}_m k_{m,\beta} + \bar{k}_f k_{f,\beta} \tag{17}$$

where $\bar{k}_m$ and $\bar{k}_f$ are, respectively, the absolute matrix and fracture permeabilities in an averaged (continuum) sense, and $k_{m,\beta}$ and $k_{f,\beta}$ are the corresponding relative permeabilities in matrix and fractures. The effective permeability can be written as a product of an absolute and a relative permeability. If relative permeability is normalized to the total absolute permeability $\bar{k}_m + \bar{k}_f$ of the fractured medium, we have

$$k_{\beta,\,\mathrm{eff}} = (\bar{k}_m + \bar{k}_f)\,.\,k_\beta \tag{18}$$

where the effective continuum relative permeability

$$k_\beta = \frac{\bar{k}_m k_{m,\beta} + \bar{k}_f k_{f,\beta}}{\bar{k}_m + \bar{k}_f} \tag{19}$$

varies between 0 and 1. Alternatively, we can write

$$k_{\beta,\,\mathrm{eff}} = \bar{k}_m \hat{k}_\beta \tag{20}$$

where the relative permeability

$$\hat{k}_\beta = k_{m,\beta} + \frac{\bar{k}_f}{\bar{k}_m} k_{f,\beta} \tag{21}$$

is now normalized to matrix permeability. With values of $\bar{k}_f/\bar{k}_m$ typically in the range of 10^3 - 10^4 (see Table 1), relative permeability then can attain very large values.

Now consider a composite medium. For simplicity of notation, assume that there is a contact between an effective continuum and a porous medium, the latter having absolute permeability $\bar{k}$ and relative permeability $k_{r\beta}$. Also, for simplicity, assume that nodal distances are the same on either side of the interface. The harmonic weighting for absolute permeability at the interface is then dependent upon the normalization adopted for the relative permeability of the effective continuum. Indeed, for the normalization with respect to the total absolute permeability $\bar{k}_m + \bar{k}_f$ we have

$$\frac{2}{k_i} = \frac{1}{\bar{k}_m + \bar{k}_f} + \frac{1}{\bar{k}} \tag{22}$$

while for the normalization to matrix permeability the absolute interface permeability is

$$\frac{2}{\hat{k}_i} = \frac{1}{\bar{k}_m} + \frac{1}{\bar{k}}. \tag{23}$$

Harmonic weighting of two permeabilities that differ by a large factor is always dominated by the smaller permeability; i.e., the harmonically weighted permeability is close to the smaller of the two. Under typical conditions where $\bar{k}_f \approx \bar{k} \gg \bar{k}_m$, it is seen that k_i is of similar magnitude as $\bar{k}_f$ (and $\bar{k}$), while $\hat{k}_i$ is of similar magnitude as $\bar{k}_m$ (and thus small compared to $\bar{k}_f$). If flow is from the porous to the fractured medium, upstream-weighted relative permeability is $k_{r\beta}$ in either case, so that the resulting effective interface permeabilities for the alternate conventions Equations (22) and (23) would be vastly different (recall that $\bar{k}_f/\bar{k}_m$ is typically of order $10^3 - 10^4$). A similar ambiguity in the definition of effective interface permeability arises when flow is from the fractured to the porous medium.

6.4. Interpretation of Anomalous Fluxes and Pressure Gradients

The very large gas pressure gradients at the 125 m and 500 m elevations (see Figure 9) are now explained as follows. At either elevation, gas flows from a nonwelded (porous) unit below to a welded (fractured) unit above (see Figures 5, 11). In the nonwelded unit, the absolute porous medium permeability is $1.8 \times 10^{-14}\,m^2$ and the

relative permeability is on the order of 1. In the welded unit, the absolute permeability of the matrix is $1.9 \times 10^{-18}\,m^2$, and the gas flow which takes place in the fracture has a relative permeability of about 10^4, when normalized to the matrix absolute permeability. With these values of absolute permeability and relative permeability, the effective gas phase permeability $\bar{k}k_{rg}$ yields similar values in either the welded or nonwelded unit (see Figure 11). However, harmonic averaging of the absolute permeabilities will be dominated by the lower value, which is that of the welded unit ($1.9 \times 10^{-18}\,m^2$), yet the relative permeability of the upstream block in the nonwelded unit is only on the order of 1, instead of $\approx 10^4$ in the welded unit, making the value of $k_i k_{rg} \approx 1.9 \times 10^{-18}$, four orders of magnitude lower than in either the welded or unwelded unit. In order to compensate for the small $k_i k_{rg}$, and in order to satisfy the flux continuity, the simulated results give the artificially large pressure gradient at the interfaces 125 m and 500 m elevation as shown in Figure 9.

A completely analogous consideration explains the large flow resistance encountered by liquid phase as it flows from a non-welded to a welded unit at the 450 m elevation level. The product $k_i k_{rl}$ from the harmonic average of absolute permeabilities and the upstream relative permeability gives rise to an artificially large resistance to liquid flow. The downward liquid flux here arises entirely from condensation of upward vapor flux in this natural state calculation, hence the dip in the liquid flux (through subtle coupling by the vapor pressure lowering effect) causes also a dip in vapor flux at 450 m as shown in Figure 8.

6.5. Does Explicit Fracture-Matrix Treatment Cure the Problem?

The discussions above show that in order to avoid the artificially large resistance to fluid flow at an interface between a fractured medium and a porous medium there must not be a discontinuity of several orders of magnitude in relative permeabilities. To achieve this we have modified the numerical simulator TOUGH to explicitly take into account, at the welded (fractured medium) and the nonwelded (porous medium) interface, whether the flow is in the fracture or matrix for each phase in the fractured welded block, and in each case the relative permeability is defined with respect to either fracture absolute permeability or matrix absolute permeability so that it is normalized to 1 in all possible flow scenarios. We therefore adopt an explicit fracture and matrix description at the stratigraphic interface. The documentation of this approach is included in Appendix A. Calculations were repeated with the above modifications

incorporated in the TOUGH simulator. The resultant fluid fluxes in Figure 12a show that the flux anomaly at the 450 m elevation as shown in Figure 8 has been removed. The resultant gas pressure profile in Figure 12b shows that the gas pressure slope discontinuities present in Figure 9 have also been corrected. In Figure 13 we show the liquid saturation profile, which differs very slightly from that shown in Figure 5b, where the effective continuum approximation was used for the fractured medium. Thus, for the particular flow problem studied here, adoption of an explicit matrix-fracture representation has succeeded in eliminating the spurious flow resistances at lithologic contacts between fractured and porous units.

The flow system we are dealing with has very subtle coupling between the gas and liquid phase flow, which is illustrated by the fluxes at elevation 450 m at a fractured medium (lower) and a porous medium (upper) interface. The results in Figure 8 were obtained when an effective continuum permeability for the fractured welded unit was used, and the results in Figure 12a were obtained with explicit matrix and fracture permeabilities for the fractured medium. In Figure 14 we compare the liquid suction pressure profiles for the two schemes of handling flow at lithologic contact. In Figure 14a, the weaker suction pressure in the nonwelded unit above 450 m leads to a larger liquid pressure gradient at the interface in order to counter the artificially large flow resistance. In spite of the large liquid pressure gradient, a dip in liquid flux still occurs at 450 m in Figure 8. In Figure 14b, the suction pressure gradient at the 450 m interface is smaller than that in Figure 14a, since the artificially large flow resistance is removed in the explicit matrix-fracture description at the interface. In the absence of the artificially large resistance to liquid flow, the liquid flux in Figure 12b is about a factor of 2 larger than that in Figure 8. The liquid flow driven by suction pressure gradients is coupled to vapor diffusion driven by vapor pressure gradients through Equation (1). The stronger suction pressure in the explicit matrix-fracture scheme (Figure 14b) gives rise to a lower vapor pressure in the upper nonwelded unit, resulting in a larger vapor pressure gradient to drive the upward diffusive flux from the welded to the nonwelded unit. Our calculations show that the vapor pressure gradient is nearly twice that of the effective continuum scheme, thus confirming the difference of a factor of 2 in the vapor fluxes from the two different schemes.

The explicit matrix-fracture description at the interface works here because the fracture absolute permeability is of the same order of magnitude as the absolute permeability of the porous medium. Had the value of fracture permeability been greatly

different from the porous medium absolute permeability, the explicit matrix-fracture description would not have resolved the problem of spurious flow resistances. The harmonic weighting of the absolute permeabilities and full upstream weighting of the relative permeabilities can potentially give rise to artificially large flow resistance at the interface of two zones of very large contrast in permeabilities, even at the contact between two non-fractured porous media. Such spurious flow resistances will occur whenever a fluid phase flows from a high permeability zone of small relative permeability into a low-permeability region, because then harmonic weighting will give a small absolute permeability at the interface. Therefore, for two-phase flow in composite media in general, we are still in need of a proper scheme in the handling of interface fluxes to avoid spurious numerical problems.

6.6. Upstream Weighting Scheme for Composite Medium

Intuitively, the product $\bar{k}k_r$ of absolute and relative permeability is one entity in the flow equation (see Equation 4) and there is no physical reason to separate the absolute permeability and relative permeability and treat them differently. The problem of artificially large flow resistance at a lithologic contact described above can be resolved if upstream weighting is applied to the product of the absolute permeability and the relative permeability. The fact that upstream weighting of the absolute permeability will lead to an non-unique definition of the pressure at the interface of adjacent nodes may be tolerated based on the following physical argument for "fuzzy" lithologic contact. The adjacent nodes on two sides of a lithologic contact may be represented schematically as in Figure 15. Total upstream weighting of the effective permeability $\bar{k}k_r$ implies that for flow from medium a to b, the flow properties remain that of medium a; and for flow from medium b to a, the properties remain that of medium b, which leads to an non-unique value of pressure at the mathematical interface of a and b. Since a geologic lithologic contact is far from a mathematical plane, we feel that as long as the thickness of the "fuzzy" region (with non-unique value of pressure) is small compared with that of the formation, upstream weighting of kk_r seems physically acceptable. This intuitive physically-based-scheme of 100% upstream weighting of the effective permeability should be able to correct for any anomalies arising from artificially large flow resistance at lithologic contacts. That the total upstream weighting scheme may work for all lithologic contacts regardless of whether the adjacent units were a porous medium or a fractured porous medium is very attractive since the

upstream scheme involves only two lines of coding modification to the TOUGH simulator instead of the far more cumbersome version for explicit matrix-fracture description of the fractured medium at the interface documented in Appendix A.

The upstream weighting of effective permeabilities at lithologic contacts was implemented, and the problem was rerun. The fluxes and the gas pressure profiles are shown in Figure 16. If we overlay Figure 16 (results of total upstream weighting) on Figure 12 (explicit matrix-fracture description at lithologic contact), we would find the plots to be indistinguishable.

It appears, then, that for general non-uniform composite media in which transient two-phase flow can take place, the only way to avoid artificial flow resistances at interfaces is full upstream weighting of both absolute and relative permeability. This may also be regarded simply as upstream weighting of effective permeability $k_{eff} = \bar{k}k_r$. With this weighting scheme, some loss of accuracy at the contact between different hydrologic units will occur in regions where only single phase flow occurs. This is illustrated in Figure 17 where we show results from a single-phase flow simulation in a horizontal column consisting of of two media. Medium 1, lying between $0 < x \leq 5$, has an absolute permeability ten times smaller than that of medium 2, occupying the region $5 < x \leq 10$. The column is discretized into ten grid blocks of equal $\Delta x = 1$. Figure 17 shows the pressure variation with x for steady single (liquid) phase flow from left to right using the harmonic weighting scheme for absolute permeability (solid line) and the upstream weighting scheme (dashed line). For upstream weighting, the larger pressure gradient present in the low-permeability zone (left) extends all the way to the nodal point beyond the interface, at x=5.5. This is a modest inaccuracy, which, if desired, may be minimized by reducing the grid block size at the interface.

In summary, the somewhat disturbing but perhaps not unexpected conclusion is that there is no single interface weighting scheme that would be optimal for all conditions. The only generally applicable weighting scheme (full upstream weighting of effective phase permeability) which avoids gross errors in general two-phase flow in composite media, is less accurate for certain classes of problems (single phase flow) than schemes of more restricted applications (harmonic weighting). The applicable weighting procedures for absolute and relative permeability k and k_r at interfaces between grid blocks for different classes of flow problems are summarized in Figure 18.

7. Simulations With Humidity Boundary Conditions For Stratified Column

Incorporating the 100% upstream weighting scheme for the lithologic contacts, we proceed with simulations which include humidity boundary conditions. A relative humidity of 50% is imposed at the land surface by means of a strong capillary suction as described in section 2. The resultant steady state liquid saturation and the flux profiles are shown in Figure 19. Along the horizontal axis in Figure 19a, the positive fluxes indicate upward flow and the negative fluxes indicate downward flow. Comparing the fluxes in Figure 19a to those in Figure 16a of the natural state (reference case) indicate that there is an upward movement of liquid flux in the welded unit when the humidity boundary condition is imposed. For the top 250 m of formation, the upward flow of moisture comes almost exclusively from the vapor flow, as in the case for the welded column in Figure 3. The decrease of upward liquid flow with elevation arises, as before, from non-linear effects, since a rapid decrease of liquid relative permeability results from the lowered liquid saturation due to the humidity boundary condition. Recall that prior to imposition of humidity boundary condition the liquid saturation (Figure 13) in the nonwelded Paintbrush Canyon unit is close to the residual saturation at which permeability to liquid flow is zero, so it is not surprising that Figure 19b shows the Paintbrush Canyon to be completely dry from loss of moisture through vaporization and upward diffusive vapor flux.

As pointed out earlier, the equilibrium liquid saturation of the formation is most affected by the characteristic curves, and it will be of interest to see its effect. We employed the characteristic curves from sample #5 PTN GU3-15 for the nonwelded units and repeated the calculations for both the "reference case" as well as the case with humidity boundary conditions. The simulated results are shown in Figures 20 and 21. Figures 20 for the fluxes and liquid saturation of the natural state are to be compared to Figures 16a and 13. Note the similarity of the results for the fluxes in Figure 20a and Figure 16a, but the difference in the liquid saturation for the nonwelded units. In the Paintbrush Canyon, the liquid saturation is about 0.4 in Figure 20b as opposed to about 0.1 in Figure 16b. We have also simulated results using characteristic curves pertaining to sample #2 PTN GU4-2 and found the liquid saturation in the Paintbrush Canyon unit is about 0.6. The ambient (in situ) saturation values, as tabulated in Reference information Base (RIB version 4.000, Ch. 1 section 4, item 2, p.2, 1989), give for the welded Topopah units the value of 0.65 ± 0.19, and the nonwelded Paintbrush unit the value of 0.61 ± 0.15. Based on these values in the

RIB, it may seem that the characteristic curves from either the sample #5 PTN GU3-15 or sample #2 PTN GU4-2, which yield the higher liquid saturation in the nonwelded units, may be better choices (Wang and Narasimhan, 1988) to represent the hydrological properties of the nonwelded units, though profiles such as Figure 16a with very low liquid saturation in the nonwelded units have been more prevalent in the published reports (e.g. Narasimhan and Alavi, 1988), since the characteristic curves of the sample #1 PTN GU3-7 have commonly been used in code-verification exercises.

Results when a boundary condition of 50% humidity is imposed are given in Figure 21. Figure 21a shows again (cf Figure 19a) that, whereas in the welded unit both the liquid and vapor flow contribute to the upward transport of moisture, in the top 250 m the removal of moisture from the formation comes mostly from the vapor flow though the upward flow of liquid is not entirely zero. Figure 21b shows that nowhere in the column is the formation entirely dried up. If we examine the fluxes for the 1-D welded column with no stratigraphy (Figures 3b), and those for the stratified column with different characteristic curves (Figures 19a and 21a), it is clear that the moisture removal from the formation is all of the same order of magnitude, confirming our claim in section 3 that vapor diffusion strength is the controlling factor for the amount of moisture that is removed from the formation with a lowered humidity boundary condition.

8. Summary

Knowledge of the physical processes and parameter sensitivity studies show that moisture removal from Yucca Mountain arising from a lowered humidity of the soil gas at the land surface is controlled by vapor diffusion. With a plausible enhanced vapor diffusion strength of $\beta=1$, a moisture flux equivalent to approximately .04 mm/yr of water has been obtained for a range of characteristic curves employed. We therefore conclude from our calculations that the rate of moisture removal from vapor transport has an upper limit of about 0.1 mm/yr. Both the presence of realistic stratigraphy of alternate layers of nonwelded and welded units, and the choice of characteristics curves, have only minor effects on the magnitude of moisture removal. However, characteristic curves play a dominant role in defining the equilibrium liquid saturation profiles of the layered formation.

Our calculations for stratigraphic columns with alternate layers of nonwelded and welded units show that order-of-magnitude discontinuities in absolute and relative

permeabilities at a lithologic contact give rise to artificially large resistance to flow if one uses the usual numerical scheme of harmonic weighting of absolute permeability and upstream weighting of relative permeability. We have resolved this numerical difficulty by invoking a physically-motivated intuitive model of a "fuzzy lithologic contact", and employing a complete 100% upstream weighting of the effective permeability $k.k_r$ at all interfaces.

The emphasis in the modeling studies presented here has been on moisture redistribution processes that are mediated by gas phase flow and diffusion, and on numerical approaches for dealing with multiphase flow in layered media. We used schematic formation parameters and one-dimensional stratigraphic columns, and idealized time-independent boundary conditions, so that our results are not expected to accurately reflect the conditions at Yucca Mountain in a quantitative sense. For example, we have only examined moisture removal by vapor diffusion, while precipitation may well cause a small net downward infiltration, with major impacts on capillary suction conditions and saturation distributions. More complete process descriptions and much more site-specific detail will be needed in future modeling studies of Yucca Mountain, so that a realistic and credible site model for repository performance assessment may be developed.

9. Acknowledgments

Review and suggestions for improvement by Robert Zimmerman and Joe Wang of LBL are gratefully acknowledged. This work was carried out under U. S. Department of Energy Contract No. DE-AC03-76SF00098, administered by the DOE Nevada Office, in cooperation with the Sandia National Laboratories, Albuquerque, New Mexico.

References

Aziz, K. and T. Settari, Petroleum Reservoir Simulation, Applied Science Publishers, London, 1979.

Bird, R. B., W. E. Stewart and E. N. Lightfoot, Transport Phenomenon, p.505, J. Wiley and Sons, New York, N. Y., 1960

Cary, J. W. and S. A. Taylor, The interaction of the simultaneous diffusions of heat and water vapor, Soil Sci. Soc. Am. Proc., 26, 413-416, 1962a.

Cary J. W. and S. A. Taylor, Thermally driven liquid and vapor phase transfer of water and energy in soil, Soil Sci. Soc. Am. Proc., 26, 417-420, 1962b.

Edlefsen, N. E. and A. B. C. Anderson, Thermodynamics of soil moisture, Hilgardia, 15(2), 31-298, 1943.

Hanks, R. J., H. R. Gardner and M. L Fairbourn, Evaporation of water from soils as influenced by drying with wind or radiation., Soil Sci. Soc. Am.,Proc., 31, 593-598, 1967.

Jury W. A. and J. Letey, Jr., Water vapor movement in soil: Reconciliation of theory and experiment, Jour. Soil Sci. Am., 43(5), 823-827, 1979.

Kipp, K. L., Jr., Effect of topography on gas flow in unsaturated fractured rock-numerical simulation, Proc. Symp. on flow and transport in unsaturated fractured rock, Amer. Geophys. Union Geophsical monograph 42, ed. D. D. Evans and T. J. Nicholson, 171-176, 1987.

Klavetter, E. A. and R. R. Peters, Estimation of hydrologic properties of an unsaturated fractured rock mass, Rep. SAND84-2642, Sandia Nat. Lab., Albuquerque, N. M., 1986.

Langkopf, B., Problem Definition Memo for COVE3a Benchmarking Problem, Sandia Nat. Lab., Albuquerque, N. M., March 26, 1987.

Montazer, P. and W. E. Wilson, Conceptual hydrological model of flow in the unsaturated zone, Yucca Mountain, Nevada, U. S. Geol. Surv. Water-Resources Investigations Report 84-4345, 1984

Narasimhan, T. N. and M. Alavi, A Benchmarking Exercise Using Computer Program TRUST, SAND 88-7053, Albuquerque, NM, 1988.

Peters R. R., E. A. Klavetter, I. J. Hall, S. C. Blair, P. R. Heller and G. W. Gee, Fracture and matrix hydrologic Characteristics of tuffaceous materiaials from Yucca

Mountain, Nye County, Nevada, SAND84-1471, Sandia Nat. Lab. Albuquerque, NM, 1984, 188 PP.

Peters, R. R. and E. A. Klavetter, A continuum model for water movement in an unsaturated fractured rock mass, Water Resour. Res., 24(3), 416-430, 1988.

Philip J. R. and D. A. de Vries, Moisture movement in porous materials under temperature gradients, Tran. Am. Geophys. Unoin, 38, 222-231, 1957.

Pruess, K., Y. W. Tsang and J. S. Y. Wang, Modeling of strongly heat driven flow in partially saturated fractured porous media in Proceedings, IAH 17th International Congress on the Hydrogeology of Rocks of Low Permeability, 486-497, Univ. of Arizona, Tuscon, 1985.

Pruess, K. TOUGH Users's Guide, report LBL-20700, Lawrence Berkeley Laboratory, Berkeley, CA. June 1987.

Pruess, K., J. S. Y. Wang, and Y. W. Tsang, Effective continuum Approximation for modeling fluid and heat flow in fractured porous tuff, rep. SAND 86-7000, Sandia Nat. Lab., Albuquerque, N.M., 1988.

Pruess, K., J. S. Y. Wang and Y. W. Tsang, On thermohydrological conditions near high-level nuclear wastes emplaced in partialy saturated fractured tuff, Part 2. Effective continuum approximation, in print, Water Resour. Res., 1990.

Ross, B., A conceptual model of deep unsaturated zones with negligible recharge, Water Resour. Res., 20, 11, 1627-1629,1984.

Ross, B., Gas-phase transport of Carbon-14 released from nuclear waste into the unsaturated zone, paper presented in the 11th International Symposium on the Scientific Basis for Nuclear Waste Management, 1987.

Tsang, Y. W. and K. Pruess, A study of thermally induced convection near a high-level nuclear waste repository in partially saturated fractured tuff, Water Resour. Res., 23 (10), 1958-1966, 1987.

Tsang, Y. W. and K. Pruess, Preliminary studies of gas phase flow effects and moisture migration at Yucca Mountain, Nevada, report LBL-28819, Lawrence Berkeley Laboratory, Berkeley, CA., 1989.

Van Genuchten, R., Calculating the unsaturated hydraulic conductivity with a new close form analytical model, Water Resour. Bull., Princeton University Press, Princeton University, Princeton, NJ., 1978.

Vargaftik, N. B., Tables on the thermophysical properties of liquids and gases, 2nd ed., John Wiley, NY, 1975.

Verma, A. K., Effects of phase transformation on steam-water relative permeabilities, Ph. D. Thesis, University of California, Berkeley, CA, (also: report LBL-20594 Lawrence Berkeley Laboratory, Berkeley, CA), 1986.

Von Konynenburg, R. A., C. F. Smith, H. W. Culham and C. H. Otto, Jr., Behavior of Carbon-14 in waste packages for spent fuel in a repository in tuff, in Scientific Basis for Nuclear Waste Management, vol. 8, ed. by C. M. Jantzen et al., Materials Research Society, Pittsburg, Pa., 1985.

Von Konynenburg, R. A., C. F. Smith, H. W. Culham and H. D. Smith, Carbon-14 in waste packages for spent fuel in a tuff repository, UCRL REP. 94708, Lawrence Livermore Nat. Lab., Livermore, Calif., 1986.

Walker, W. R., J. D. Sabey and D. R. Hampton, Studies of Heat Transfer and Water Migration in Soils, Final report, Department of Agricultural and Chemical Engineering, Colorado University, Fort Collins, CO, April 1981.

Wang, J. S. Y. and T. N. Narasimhan, Hydrologic modeling of vertical and lateral movement of partially saturated fluid flow near a fault zone at Yucca Mountain, report SAND87-7070, Sandia Nat. Lab., Albuquerque, N.M., 1988.

Weeks, L. V., S. J. Richards and J. Letey, Water and salt transfer in soil resulting from thermal gradients, Soil Sci. Soc. Am. Proc., 32, 193-197, 1968.

Weeks, E. P. and W. E. Wilson, Preliminary Evaluation of hydrologic properties of cores of unsaturated tuff, test well USW H-1, Yucca Mountain, Nevada, U. S. Geol. Surv. Water Resources Investigations Report 84-4193, 1984.

Weeks, E. P., Effect of topography on gas flow in unsaturated rock-concepts and observations, Proc. Symp. on flow and transport in unsaturated fractured rock, Amer. Geophys. Union Geophsical monograph 42, ed. D. D. Evans and T. J. Nicholson, 165-170, 1987.

APPENDIX A
Explicit Description of Matrix and Fracture Fluid Flow at a Lithologic Contact Between a Fractured and a Porous Medium

In the effective continuum approximation, one set of hydrologic parameters is defined for the description of fluid flow in the fractured porous medium. In order to describe matrix and fracture flow explicitly at the interface of a fractured and a porous medium, separate parameters for the matrix and the fracture media, denoted by subscripts m and f, need to be defined.

(1) Threshold liquid saturation

Let S_l be the liquid saturation of the effective continuum. It is expressed in terms of the matrix and fracture saturations as follows (Pruess et al., 1988):

$$S_l = \frac{S_{lm}\bar{\phi}_m + S_{lf}\bar{\phi}_f}{\bar{\phi}_m + \bar{\phi}_f} \tag{A-1}$$

where both $\bar{\phi}_m$ and $\bar{\phi}_f$ are void fractions defined relative to the total volume,

$$V_{tot} = V_m + V_f \,. \tag{A-2}$$

Total effective porosity is $\bar{\phi} = \bar{\phi}_m + \bar{\phi}_f$. The threshold saturation, S_{th}, is defined as the continuum liquid saturation at the juncture when the matrix is fully saturated and the fracture is dry, that is, S_{th} is the value of S_l in Equation (A-1) where S_{lm} is 1 and S_{lf} is 0,

$$S_{th} = \frac{\bar{\phi}_m}{\bar{\phi}_m + \bar{\phi}_f} = 1 - \frac{\bar{\phi}_f}{\bar{\phi}} \,. \tag{A-3}$$

For the values of $\bar{\phi} = .10$ and $\phi_f = .00177$ as tabulated in Table 1, we have $S_{th} = 0.9823$. The reasoning which leads to the definition of threshold liquid saturation is as follows. An effective continuum concept is only applicable when approximate local thermodynamic equilibrium exists between matrix and fractures. Because the capillary suction in the matrix is much stronger than that in the fractures, local equilibrium implies that liquid saturation in the fractures will remain near zero until matrix satuation approaches 100%. The concept of a liquid threshold saturation as defined by Equation (A-3) is based on the approximation that the enormous disparity of the strength of capillary suction in the matrix and fractures will cause the fractures to remain completely dry until the matrix becomes fully saturated during imbibition; and for the fractures to be completely drained before the matrix begins to desaturate during drainage. We have found the above approximation of local equilibrium to be an excellent one from running 2-D simulations of discrete fracture and matrix systems with infiltration.

From Equation (A-1), given the liquid saturation of the effective continuum, S_l, the matrix and fracture liquid saturation are as follows:

$$S_{lm} = S_l / S_{th}, \quad S_{lf} = 0; \qquad \text{for } S_l \le S_{th}$$

$$S_{lm}=1, \quad S_{lf}=\frac{(S_l-S_{th})}{(1-S_{th})}; \qquad \text{for } S_l > S_{th} \tag{A-4}$$

(2) Harmonic weighting of absolute permeabilities and upstream weighting of relative permeabilities for matrix and fracture separately

Consider a fractured medium (FM) with absolute matrix and fracture permeabilities (in an average continuum sense) of $\bar{k}_m$ and $\bar{k}_f$, respectively. At an interface with a porous medium (PM) of absolute permeability $\bar{k}$, we can define a harmonically averaged permeability $\bar{k}_{im}$ for flow between the matrix and the porous medium, and a harmonically averaged permeability $\bar{k}_{if}$ between the fractures and the porous medium as follows (see Figure 22),

$$\frac{d_{FM}+d_{PM}}{\bar{k}_{im}} = \frac{d_{FM}}{\bar{k}_m} + \frac{d_{PM}}{\bar{k}} \tag{A-5}$$

$$\frac{d_{FM}+d_{PM}}{\bar{k}_{if}} = \frac{d_{FM}}{\bar{k}_f} + \frac{d_{PM}}{\bar{k}} \tag{A-6}$$

Here d_{FM} and d_{PM} are, respectively, the nodal distances from the interface in the fractured and porous medium. Using the scheme of harmonic weighting for absolute permeabilities, and full upstream weighting of relative permeabilities, the effective permeabilities at a FM-PM interface are as given in Table A-1.

Table A-1
Effective Permeabilities

flow direction	matrix (m)	fracture (f)
PM --> FM	$\bar{k}_{im}\, k_{r\beta}$	$\bar{k}_{if}\, k_{r\beta}$
FM --> PM	$\bar{k}_{im}\, k_{r\beta,m}$	$\bar{k}_{if}\, k_{r\beta,f}$

The subscript β stands for either gas or liquid phase, and the total effective permeability is always the sum of matrix (m) and fracture (f) contributions. Note that when the fractured medium is upstream for liquid flow, and when its liquid saturation is below the threshold saturation, (Equations A-3 and A-4), $k_{rl,f}$ in Table A-1 is 0, so that only the matrix contributes. Similarly, when the fractured medium is upstream for gas flow, and when the liquid saturation is above the threshold, then $k_{rg,m}$ is 0 and only the fracture contribution enters into Table A-1.

Table 1
Material Properties of
Welded and Nonwelded Tuff Units.

Table 1		
	Welded Units	Nonwelded Units
Rock grain density	$\rho_R = 2480$ kg/m^3	2300 kg/m^3
Rock specific heat	$C_R = 840$ J/kg C	840 J/kg C
Matrix continuum permeability	$\bar{k}_m = 1.9 \times 10^{-18}$m^2	1.8×10^{-14}m^2
Fracture continuum permeability	$\bar{k}_f = 1.8 \times 10^{-14}$m^2	--
Formation heat (a) conductivity (dry)	$K_{dry} = 1.90$ W/m C	1.02 W/m C
Formation heat (a) conductivity (fully saturated)	$K_{wet} = 2.34$ W/m C	1.35 W/m C
Total (effective) porosity	$\bar{\phi} = 0.1$	$\phi = 0.4$
Fracture porosity	$\bar{\phi}_f = .00177$	--

(a) At intermediate liquid saturation S_l, heat conductivity is $K(S_l) = K_{dry} + S_l\ (K_{wet} - K_{dry})$

Table 2
Van Genuchten's Parameters for the Characteristic Curves of Different Samples in the Nonwelded and Welded Matrix.

Table 2 Van Genuchten's Parameters for Characteristic Curves						
Sample	Ref.	S_r	$\alpha(m^{-1})$	n	$\lambda = 1 - \frac{1}{n}$	$\rho g \frac{1}{\alpha}$(MPa)*
#1 PTN GU3–7+	(a)	.1	.015	6.872	.8545	0.6526
#2 PTN GU4-2	(b)	.04	.0305	1.22	.1803	0.3210
#3 TSW G4-6	(a)	.08	.00567	1.798	.4438	1.726
#4 CHNV GU3–14+	(a)	.041	.016	3.872	.7417	0.6118
#5 CHNV GU3-15	(b)	.085	.044	1.496	.3316	0.2225
#6 TSW Fracture	(a)	.0395	1.2851	4.23	.7636	Not Used

(a) Klavetter and Peters (1986)
(b) Peters et al. (1984)
*based on $\rho = 998.2 kg/m^3$ (density of H_20 at 20 °C)
+note the similarity between samples #1 and #4.

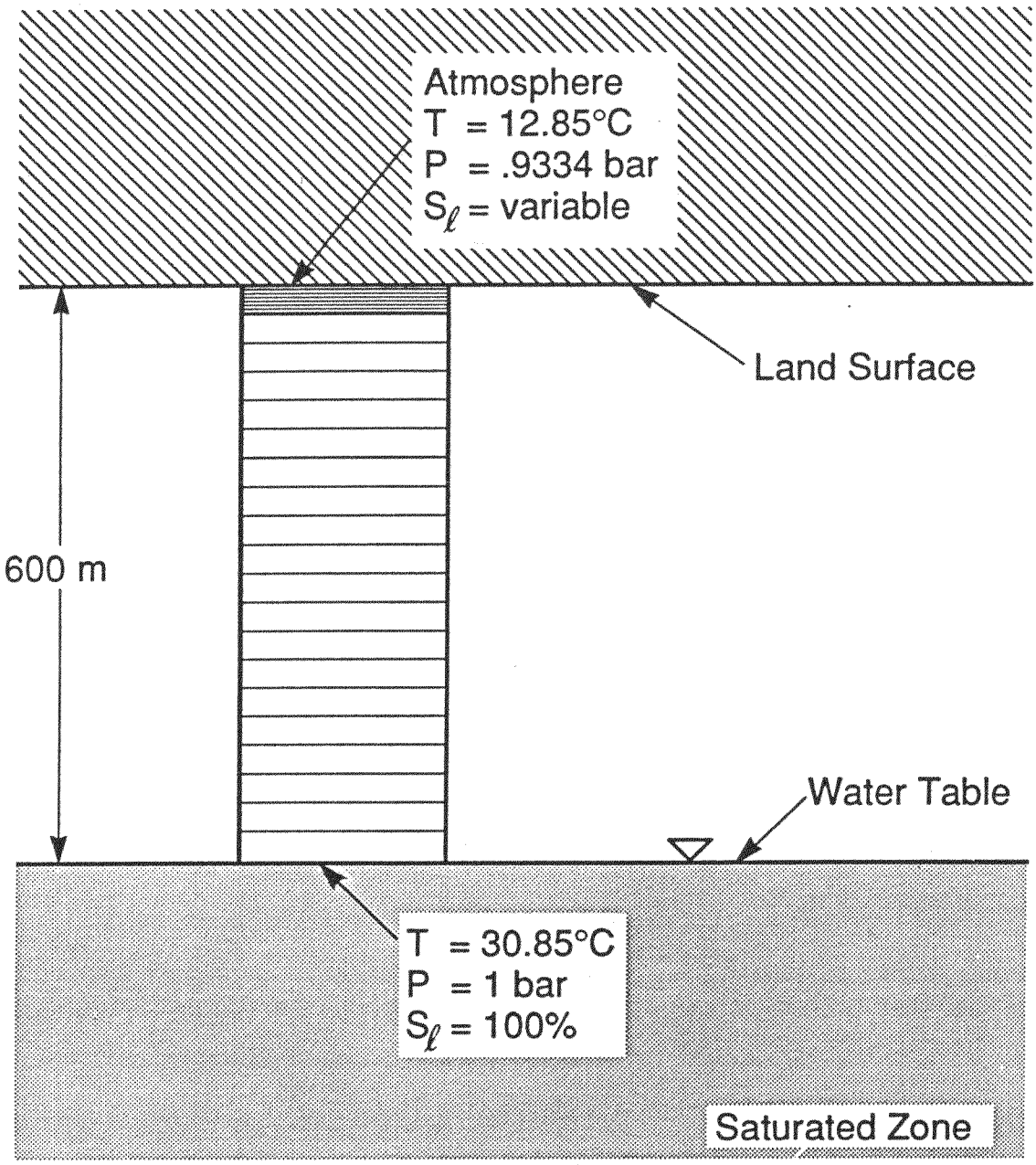

XBL 882-10033

Figure 1. One-dimensional vertical column for simulation studies of humidity effects at the land surface.

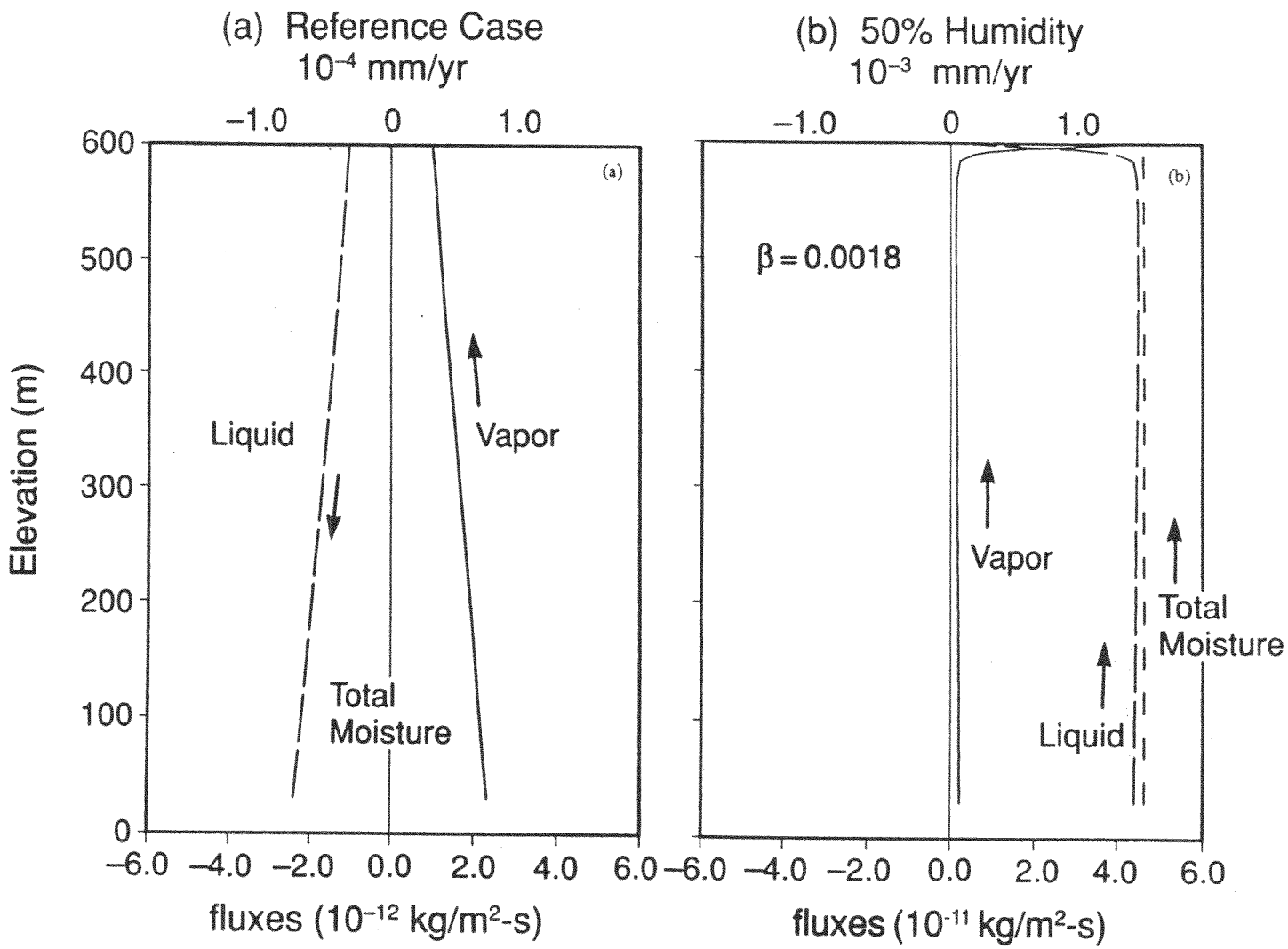

Figure 2. Fluxes in a column of welded tuff with vapor and air diffusion strength $\beta = .0018$.

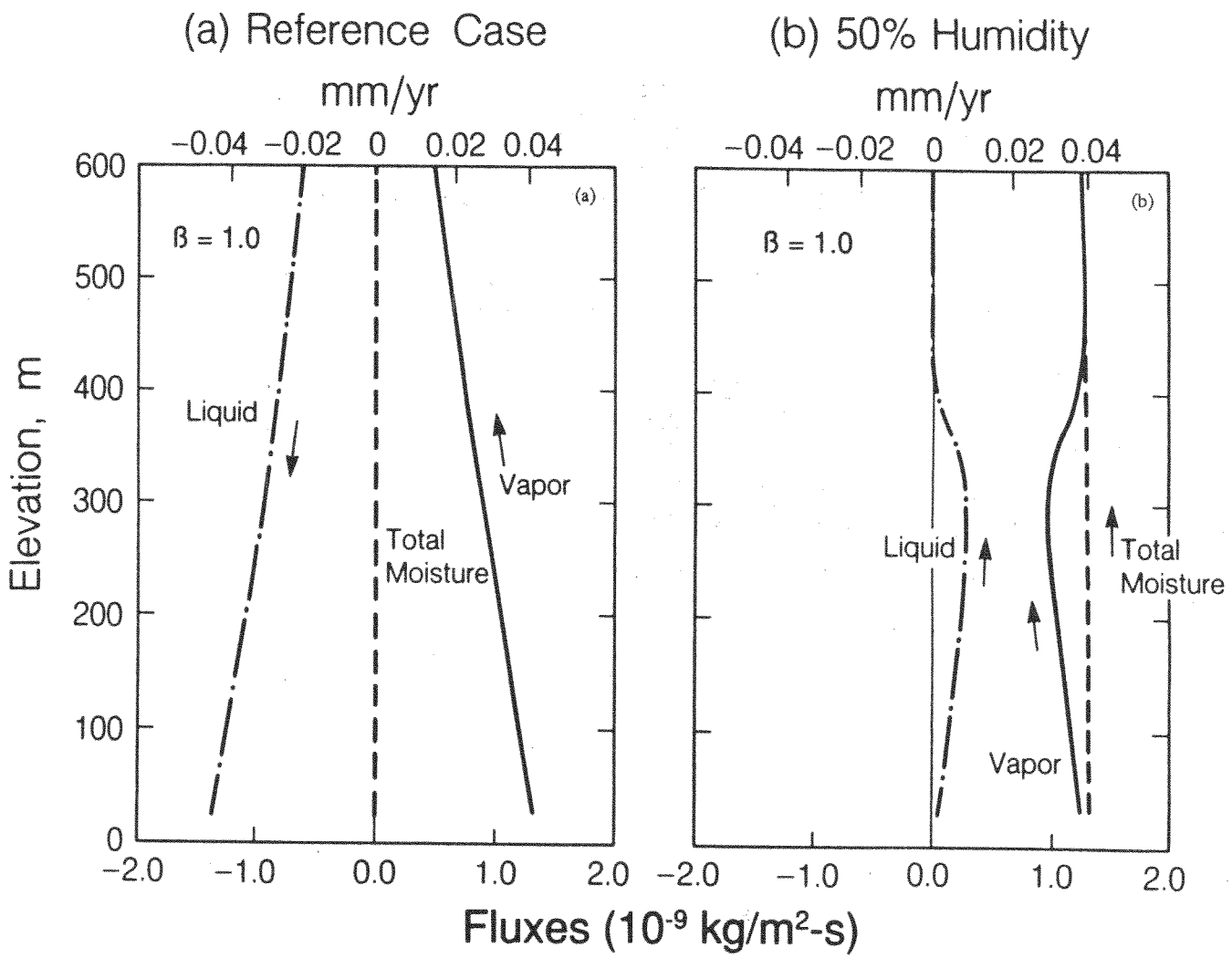

XBL 891-7440

Figure 3. Fluxes in a column of welded tuff with vapor diffusion strength $\beta = 1$, and air diffusion strength $\beta = .0018$.

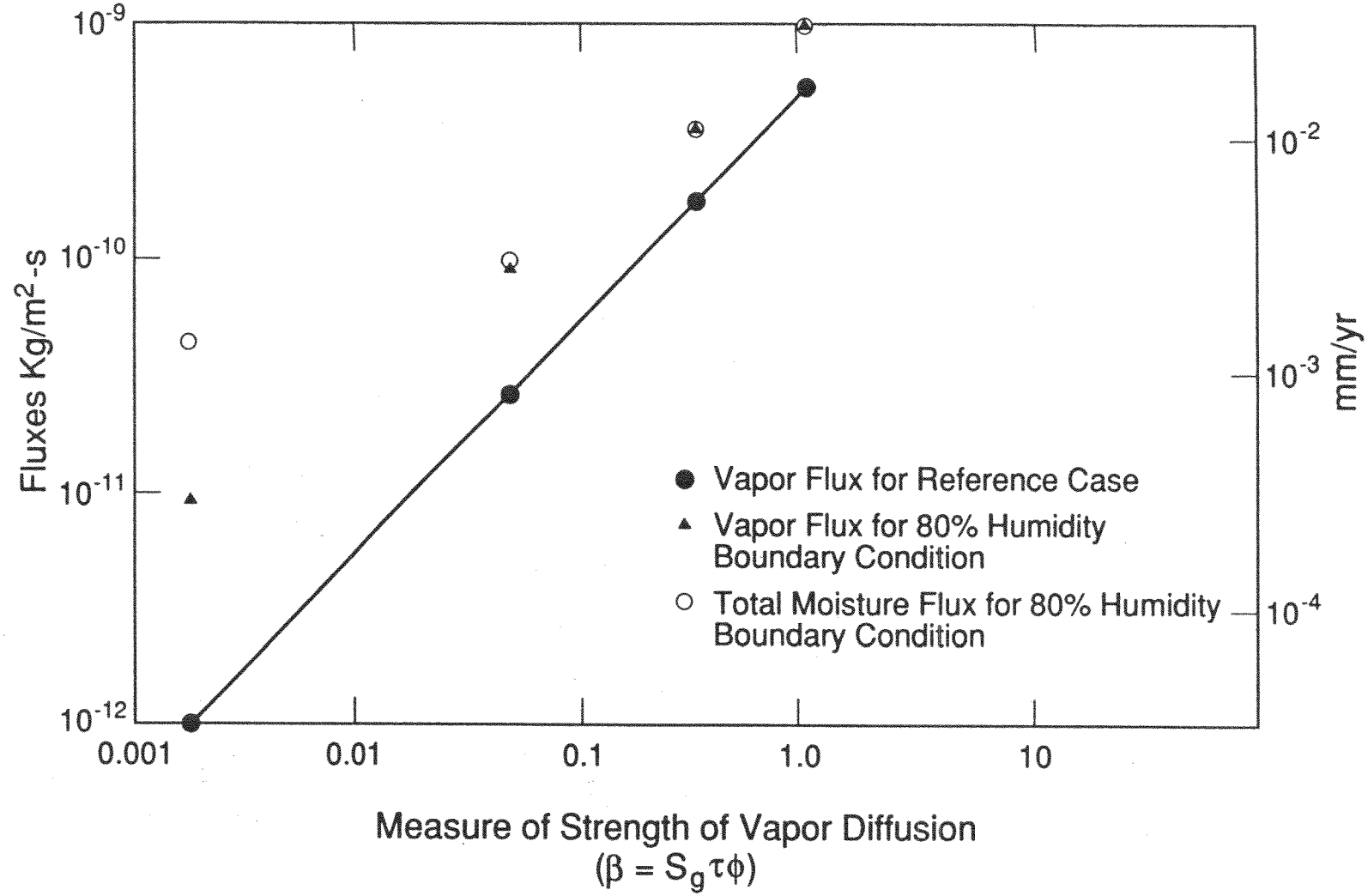

XBL 899-7751

Figure 4. Fluxes at land surface as a function of vapor diffusion strength.

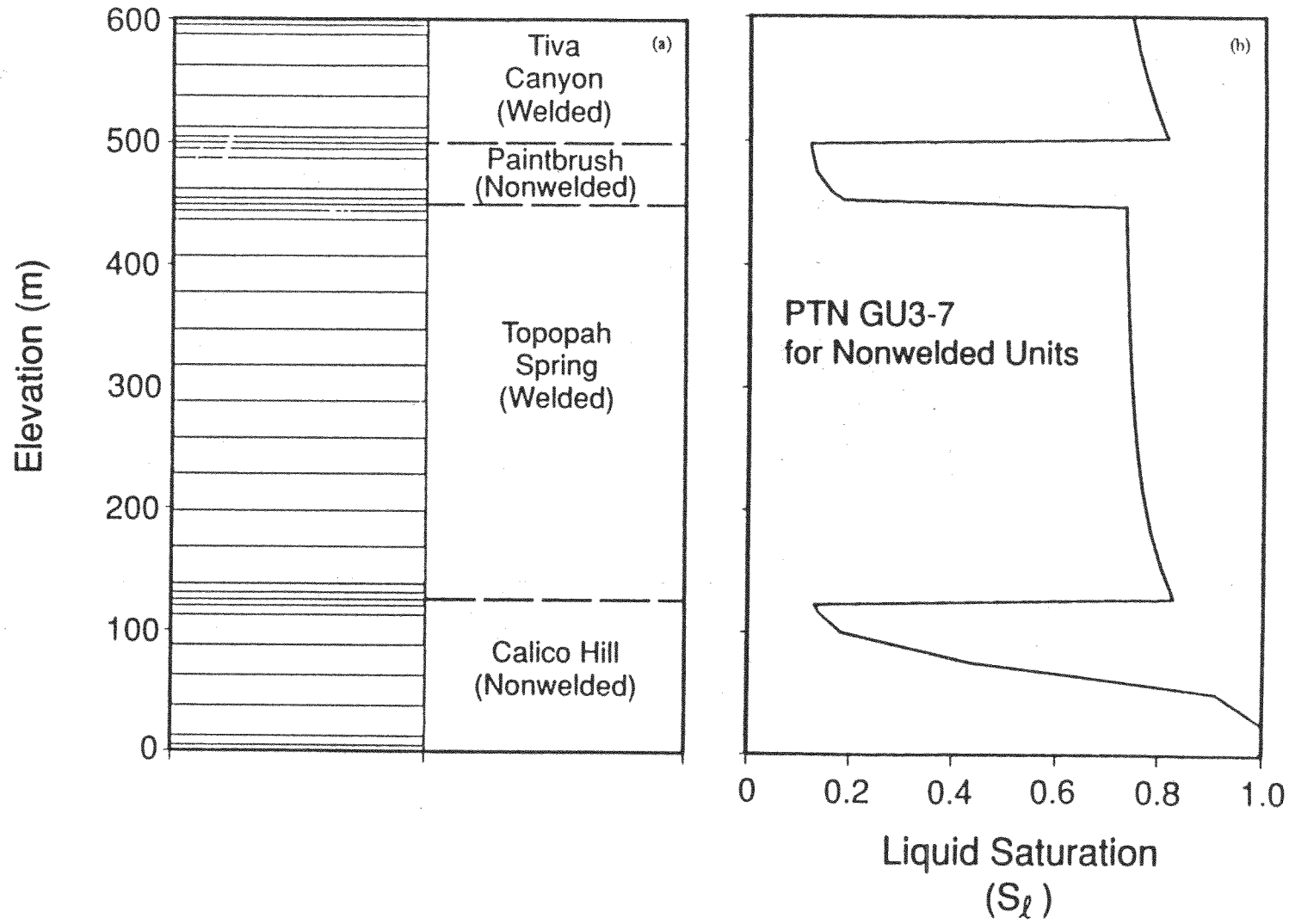

XBL 899-7750

Figure 5. (a) Division of hydrologic units and spatial discretization for numerical simulation and (b) Liquid saturation profile for a layered column of welded and nonwelded tuff.

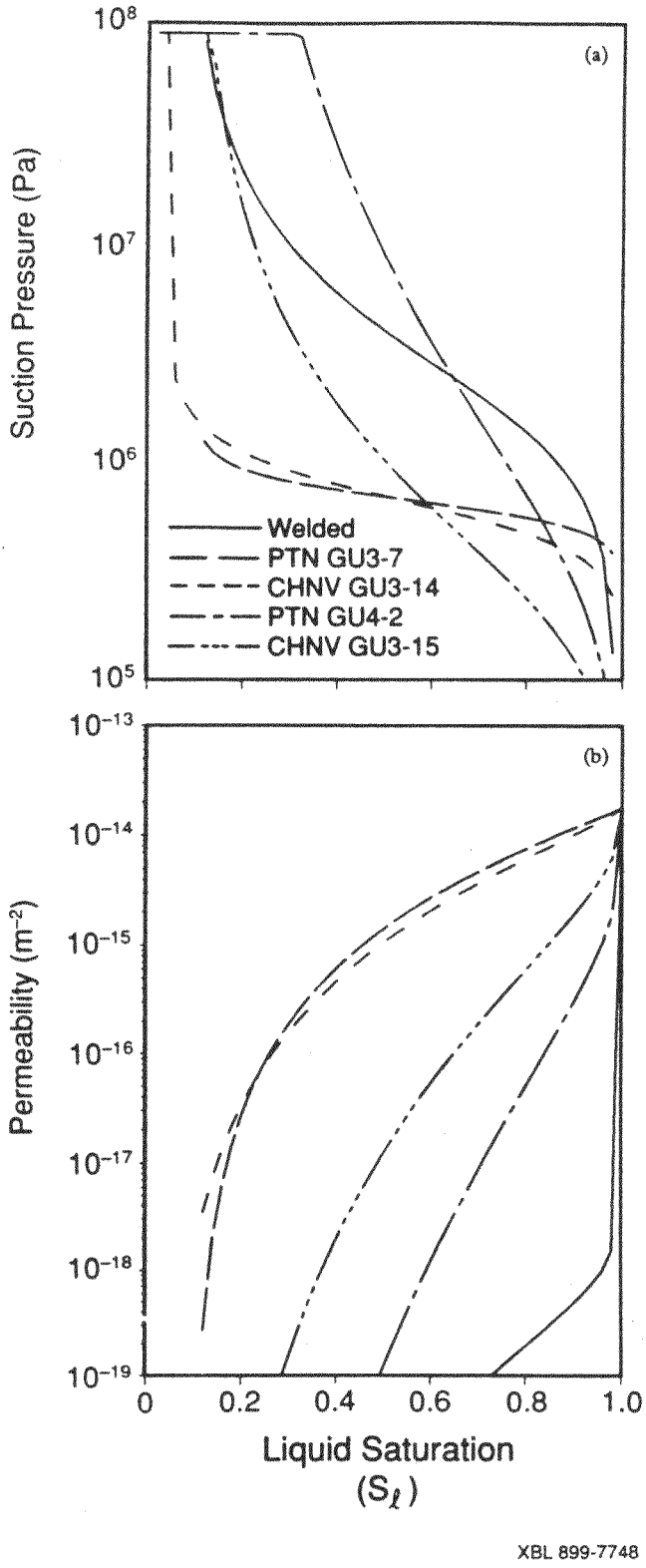

Figure 6. Characteristic curves: (a) Capillary suction, (b) Relative permeability for samples from different hydrologic units.

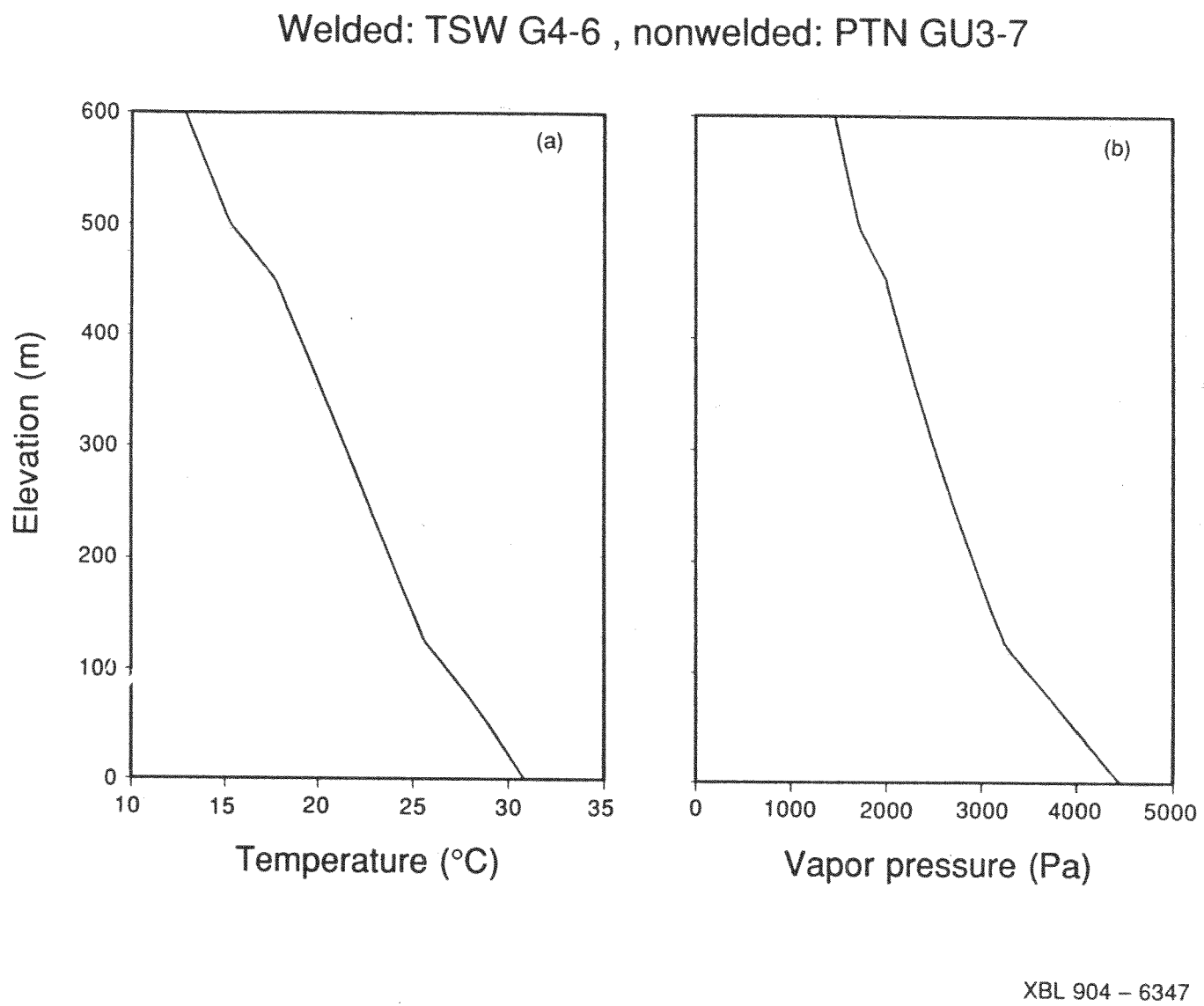

Figure 7. (a) Temperature profile and (b) Vapor pressure profile of the layered column.

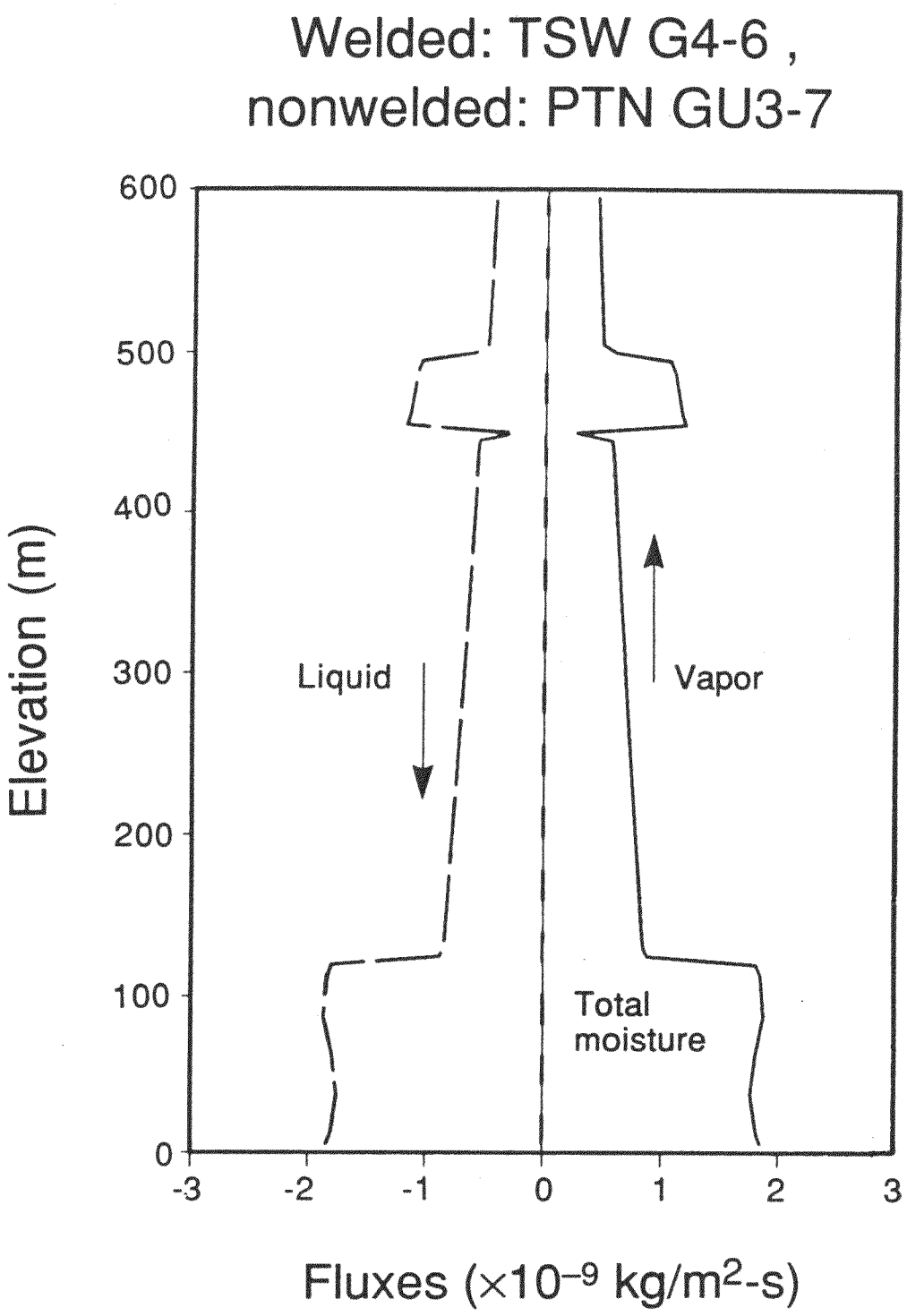

XBL 904-6351

Figure 8. Fluxes for reference case of the layered column.

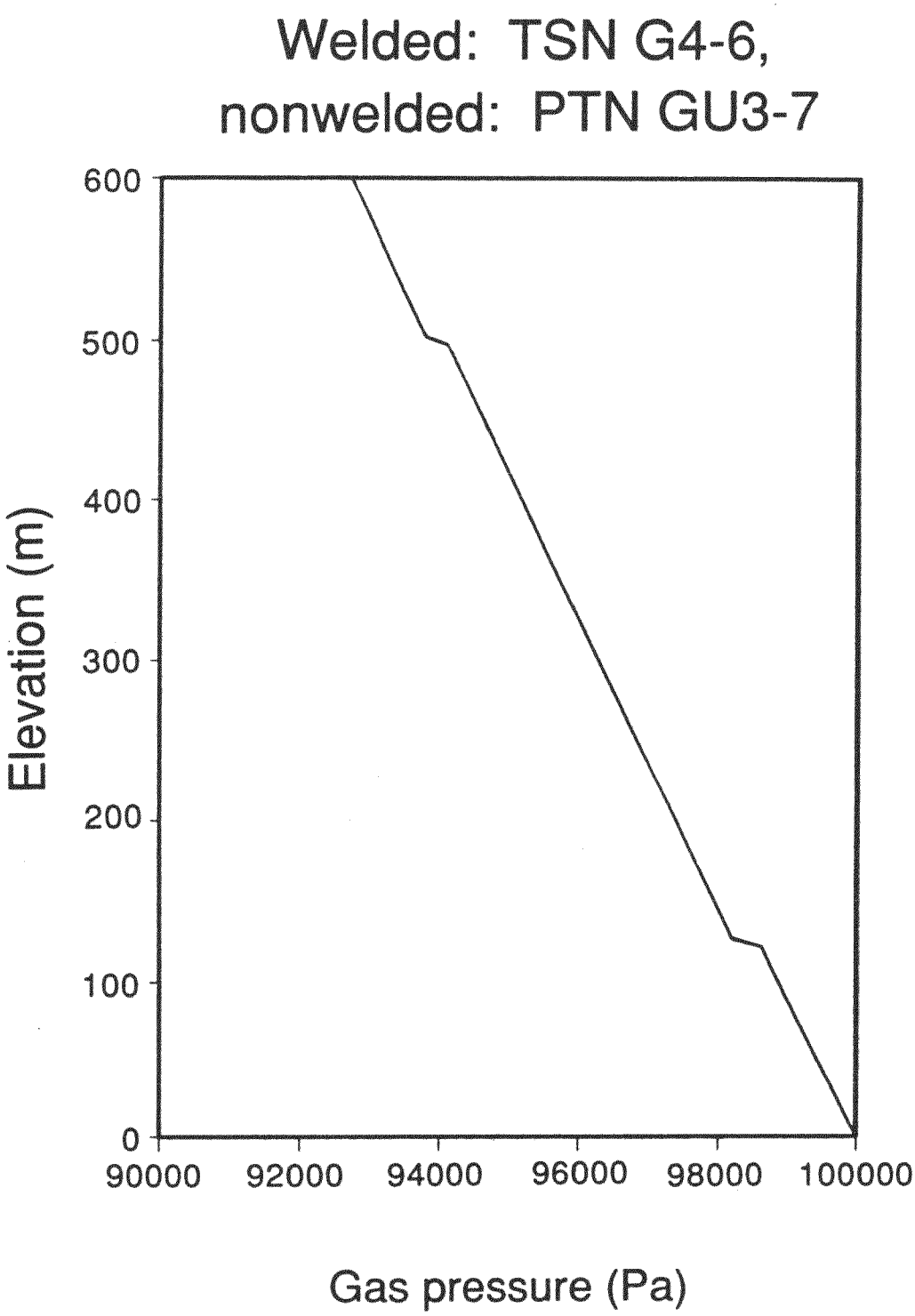

XBL 904-6352

Figure 9. Gas pressure profile of the layered column.

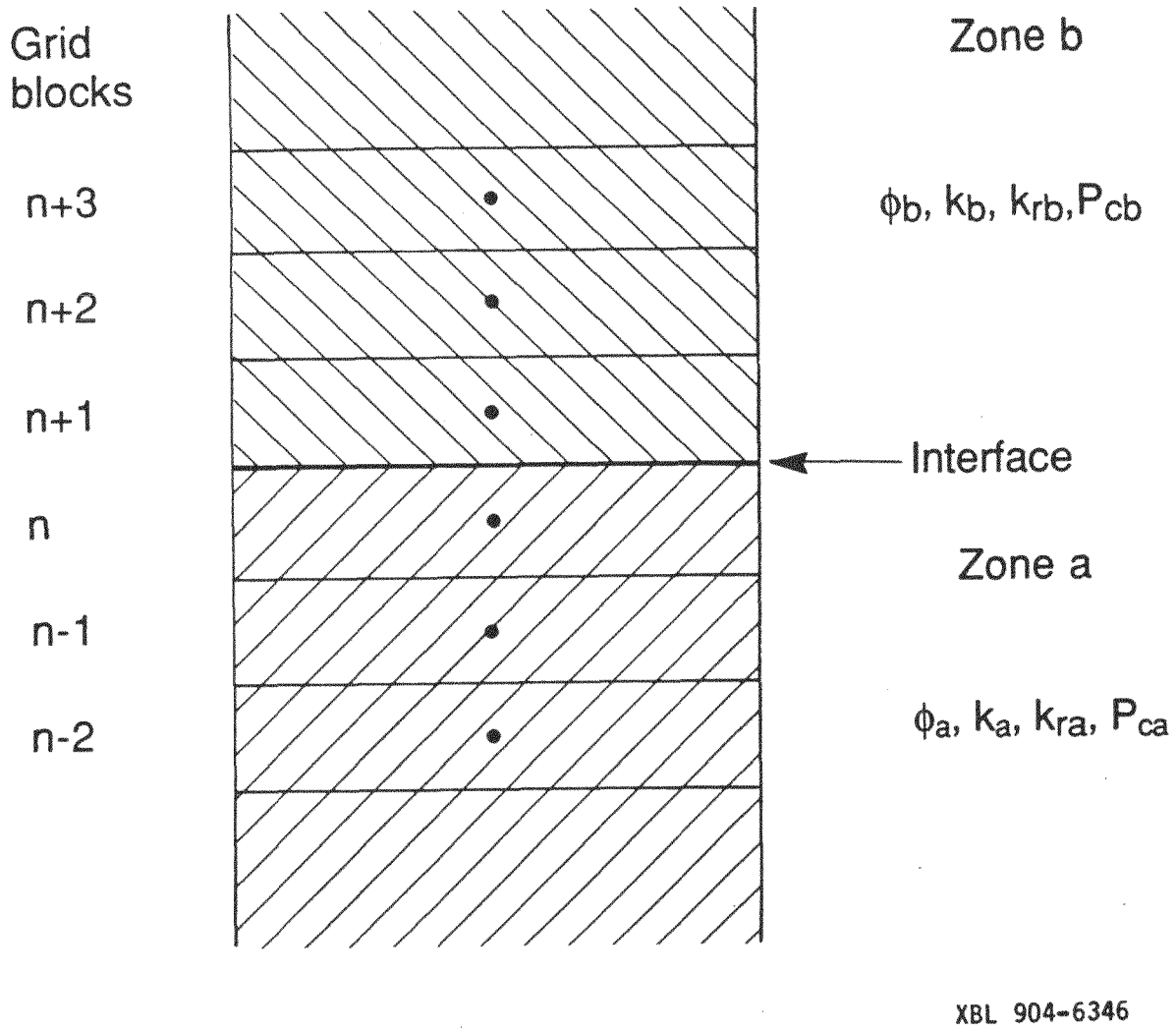

Figure 10. Schematic of a composite medium. Hydrologic parameters change discontinuously at the interface. Spatial discretization for numerical simulation of flow is also shown.

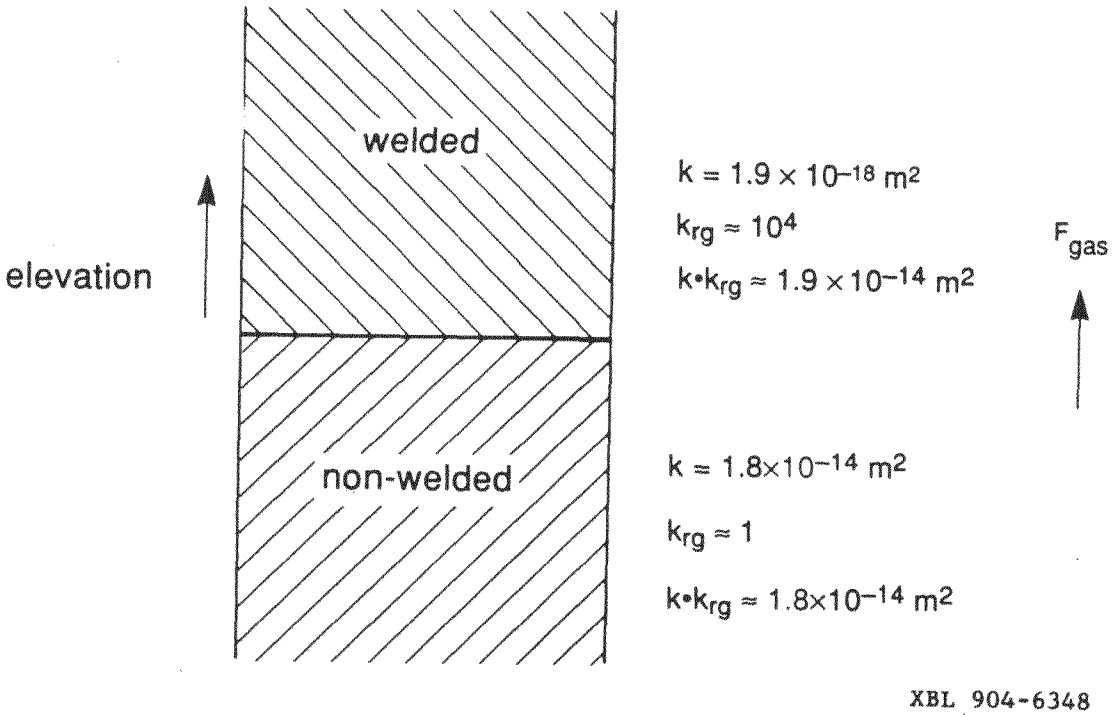

Figure 11. Typical permeability conditions for upward gas flow at a contact between a nonwelded zone (below) and a welded zone (above).

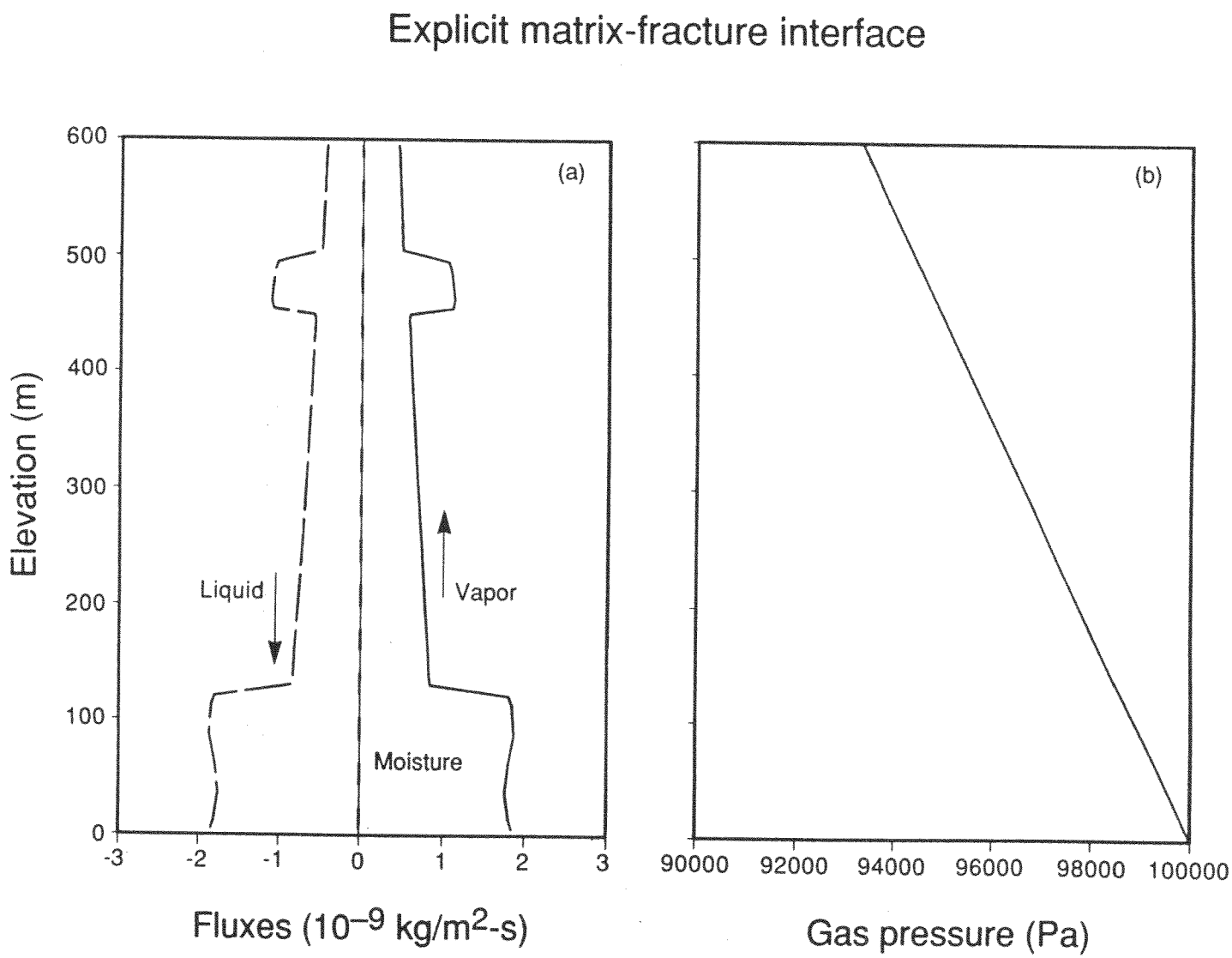

XBL 904 – 6350

Figure 12. (a) Fluxes and (b) Gas pressure profile of a layered column with the characteristic curves of GU3-7 for the nonwelded units. At the welded and nonwelded interface matrix and fracture flow are handled explicitly.

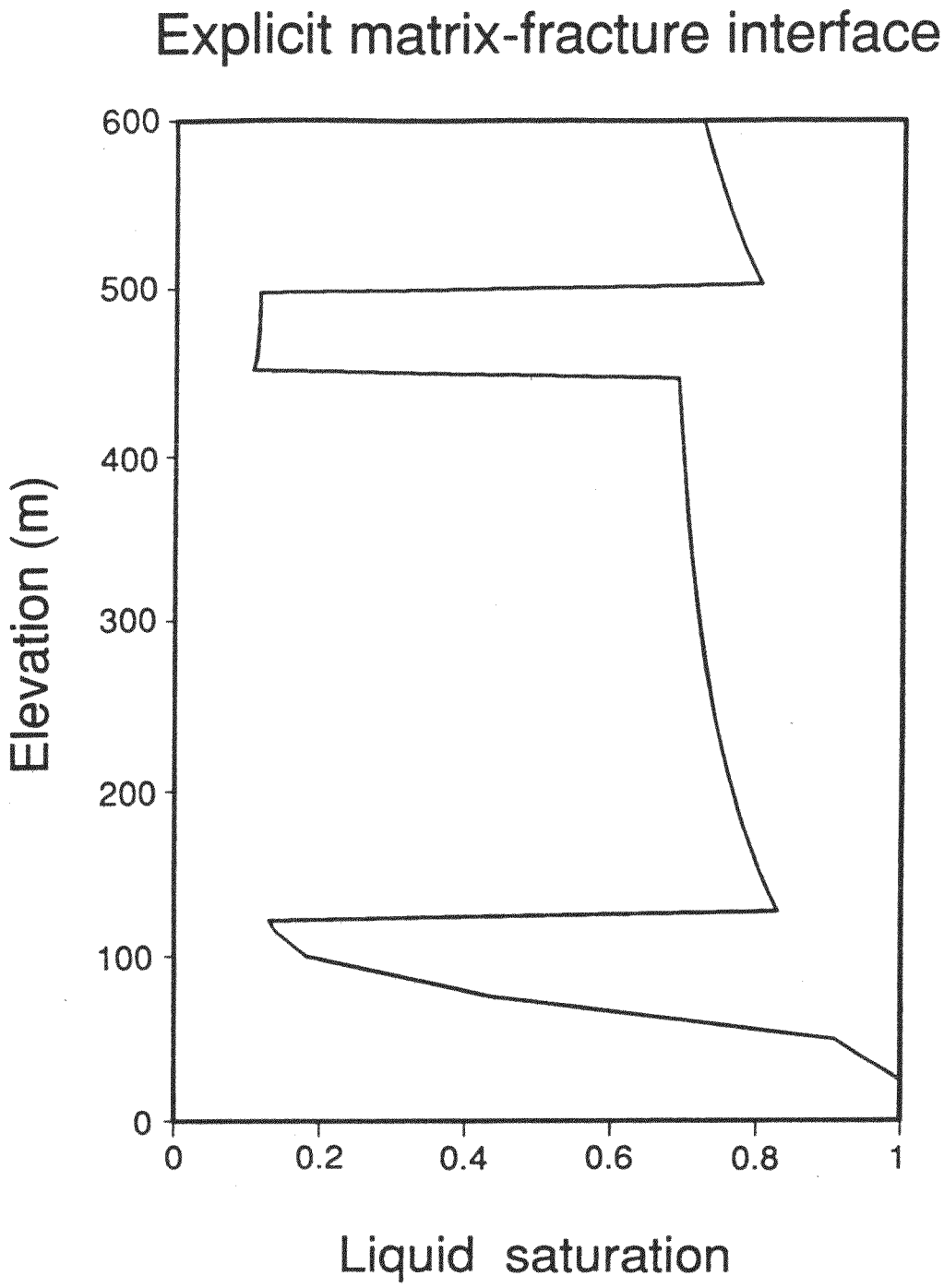

XBL 904-6349

Figure 13. Liquid saturation profile of a layered column with the characteristic curves of GU3-7 for the nonwelded units. At the welded and nonwelded interface matrix and fracture flow are handled explicitly.

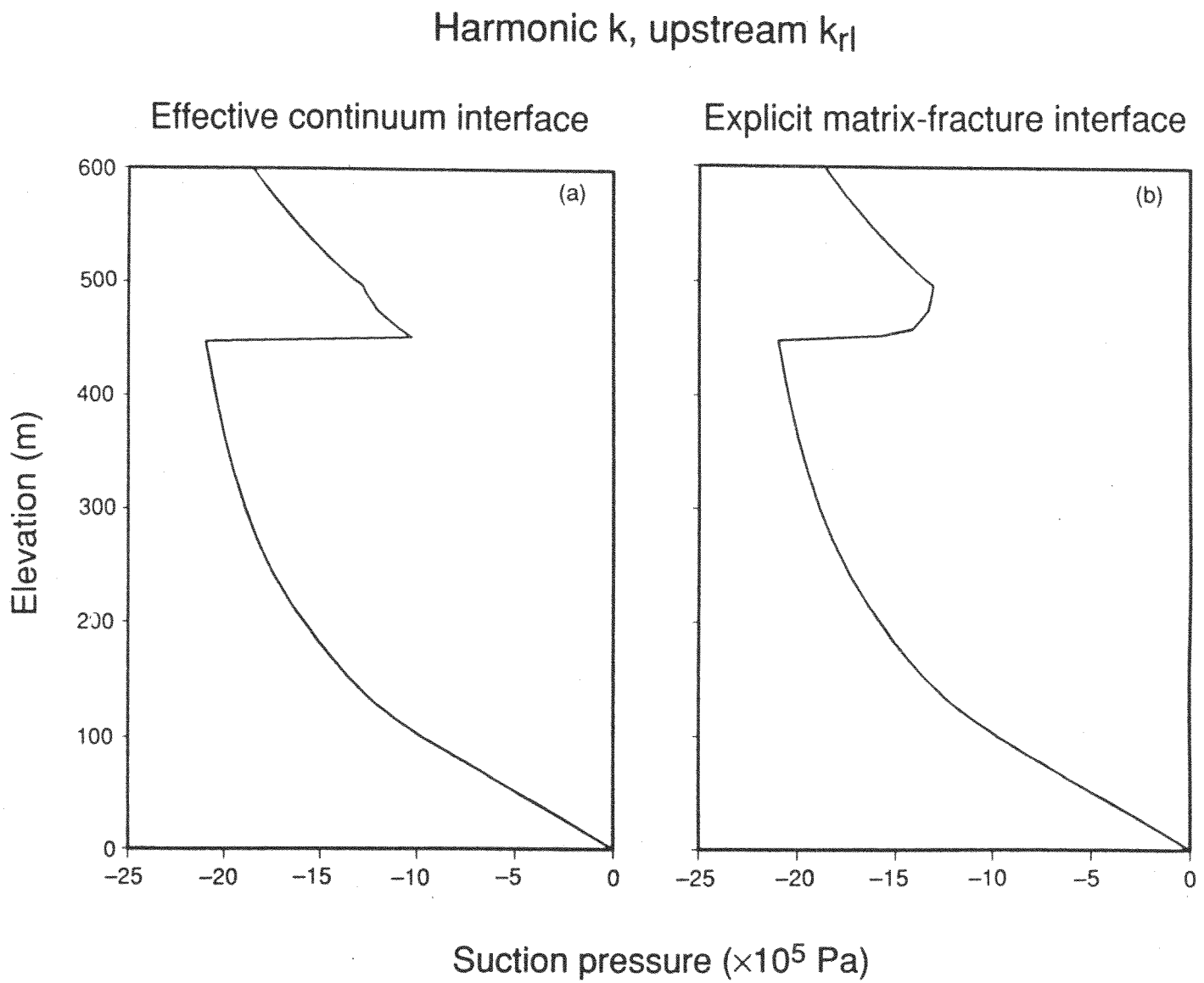

XBL 904 – 6353

Figure 14. Capillary suction pressure for a layered column using (a) effective continuum (b) explicit matrix-fracture description for the fractured medium at the interface.

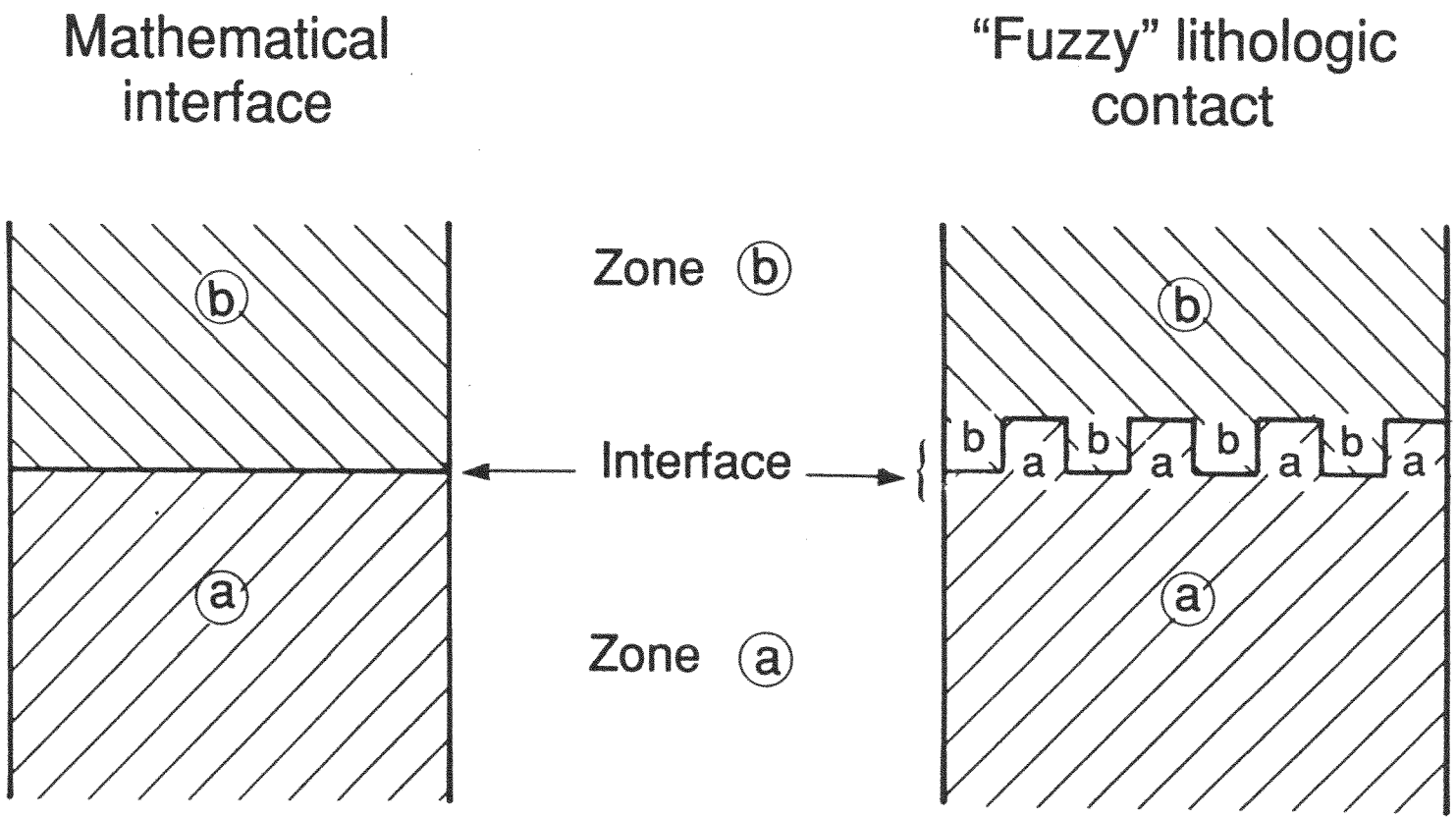

Figure 15. Schematic interface of a composite medium to illustrate total upstream weighting of effective permeability.

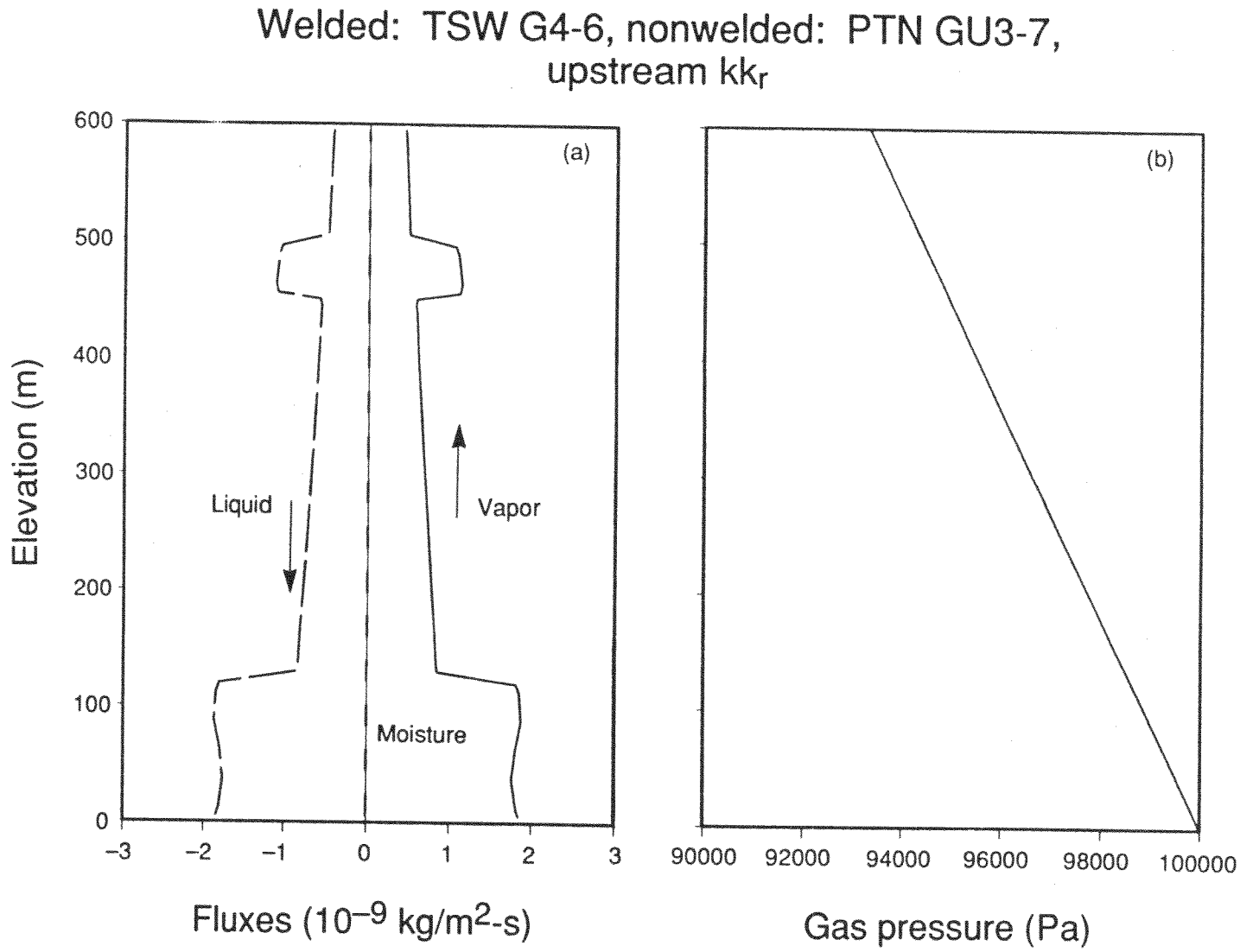

XBL 904 – 6355

Figure 16. (a) Fluxes and (b) Gas pressure profile of a layered column with the characteristic curves of GU3-7 for the nonwelded units. At the welded and nonwelded interface multiphase flows are handled by total upstream weighting of effective permeability.

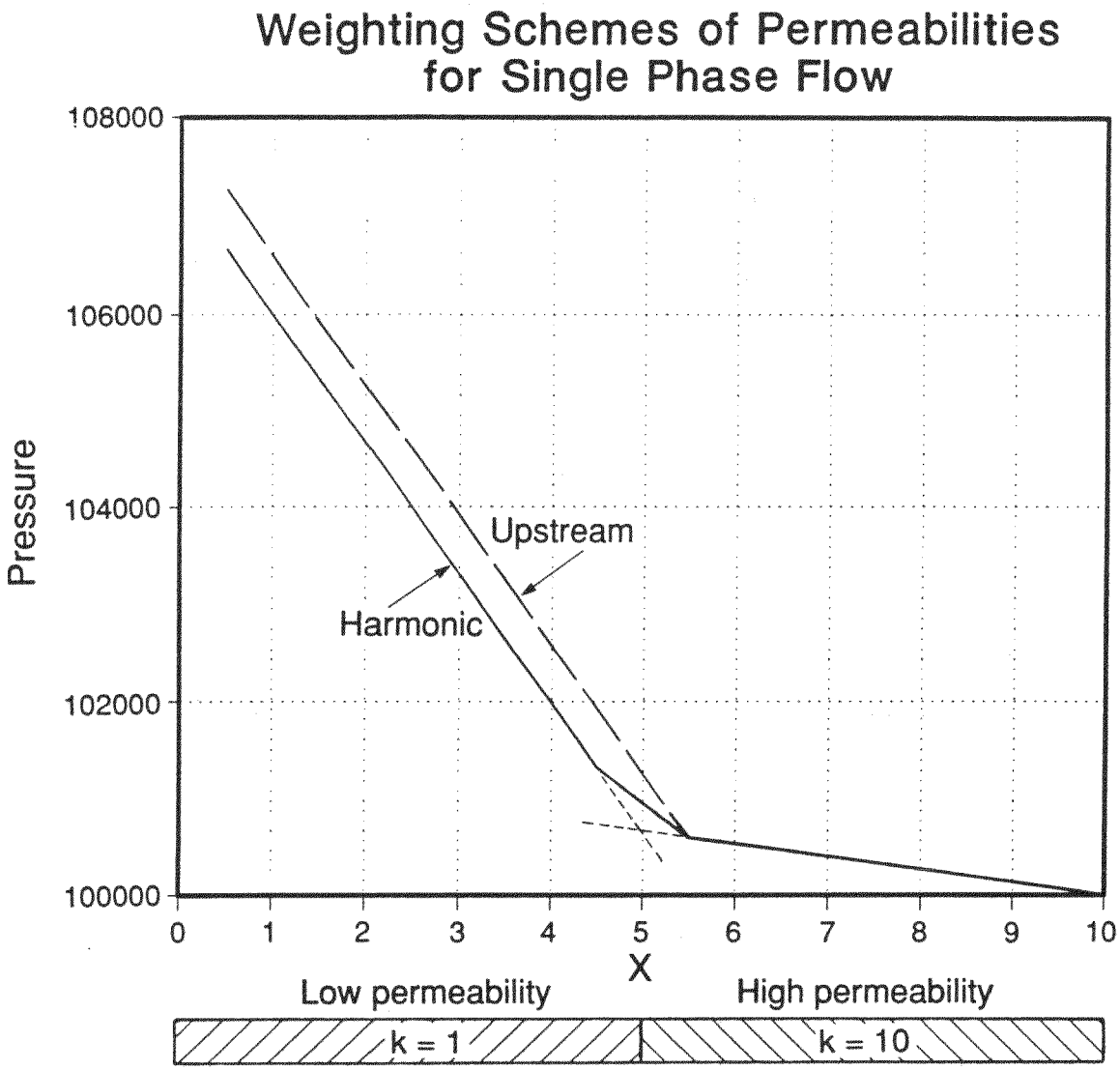

Figure 17. Pressure variation for single-phase steady-state flow with harmonic and total upstream weighting schemes for permeability.

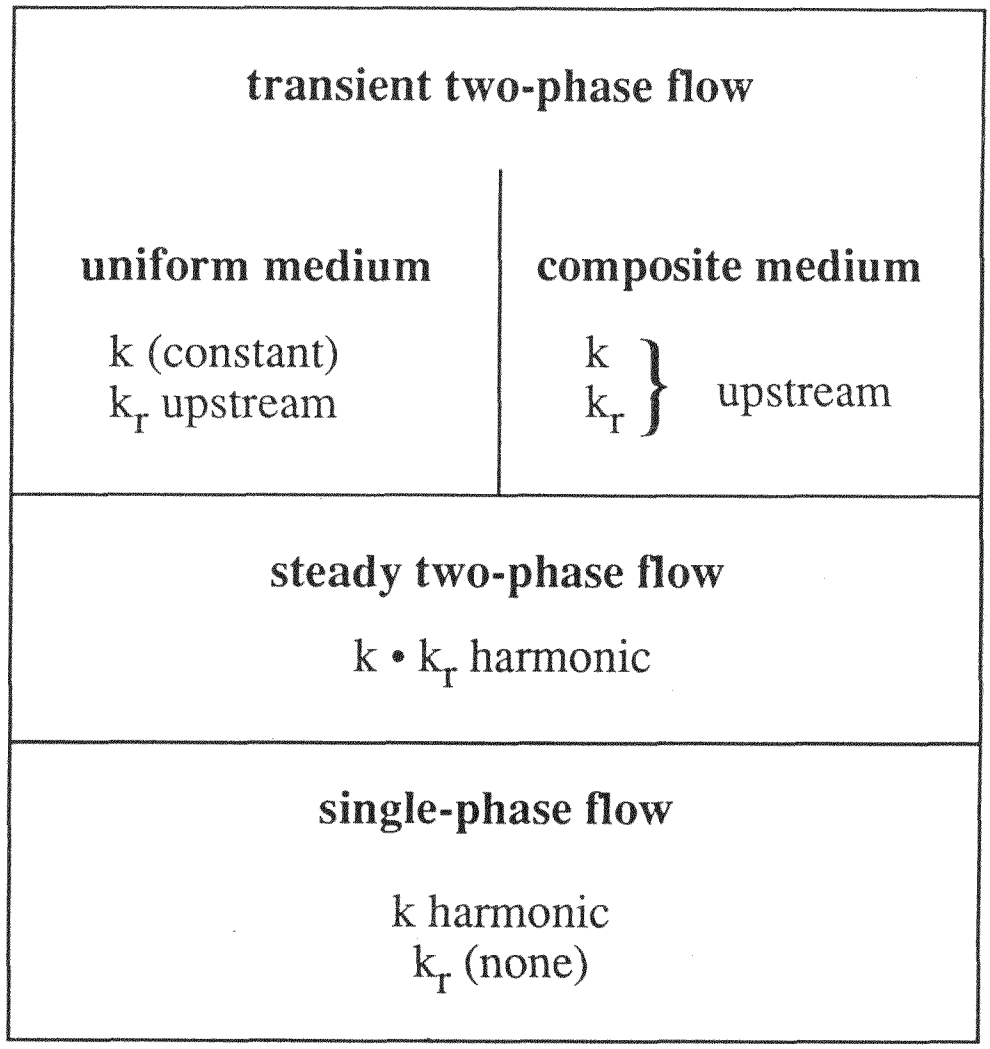

ESD-905-0007

Figure 18. Weighting procedures for absolute (k) and relative permeability (k_r) at interfaces between grid blocks for different classes of flow problems.

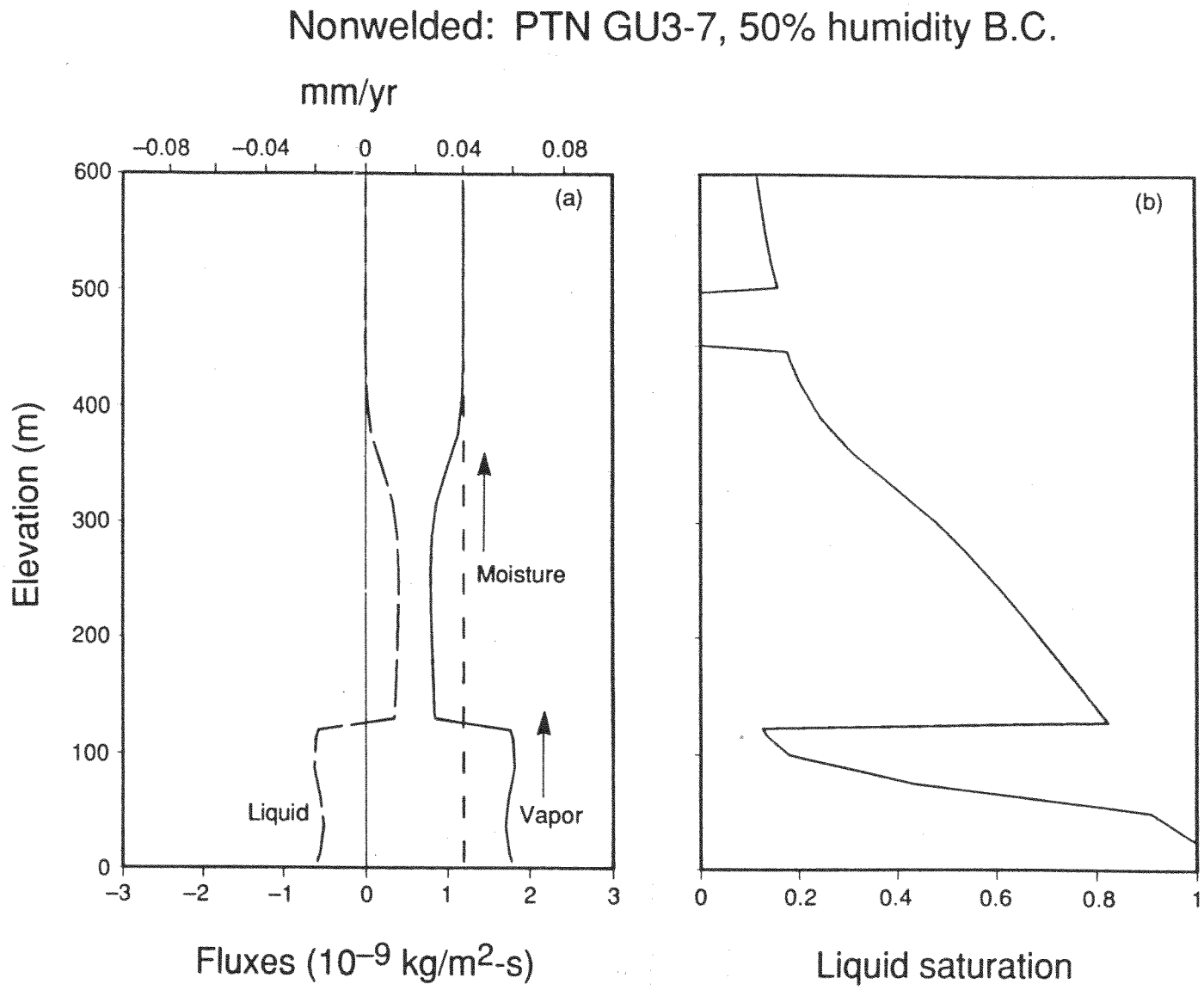

XBL 904 – 6357

Figure 19. (a) Liquid and vapor fluxes and (b) Liquid saturation profile for a layered column with 50% humidity boundary condition imposed (characteristic curves of sample #1 PTN GU3-7 for nonwelded units).

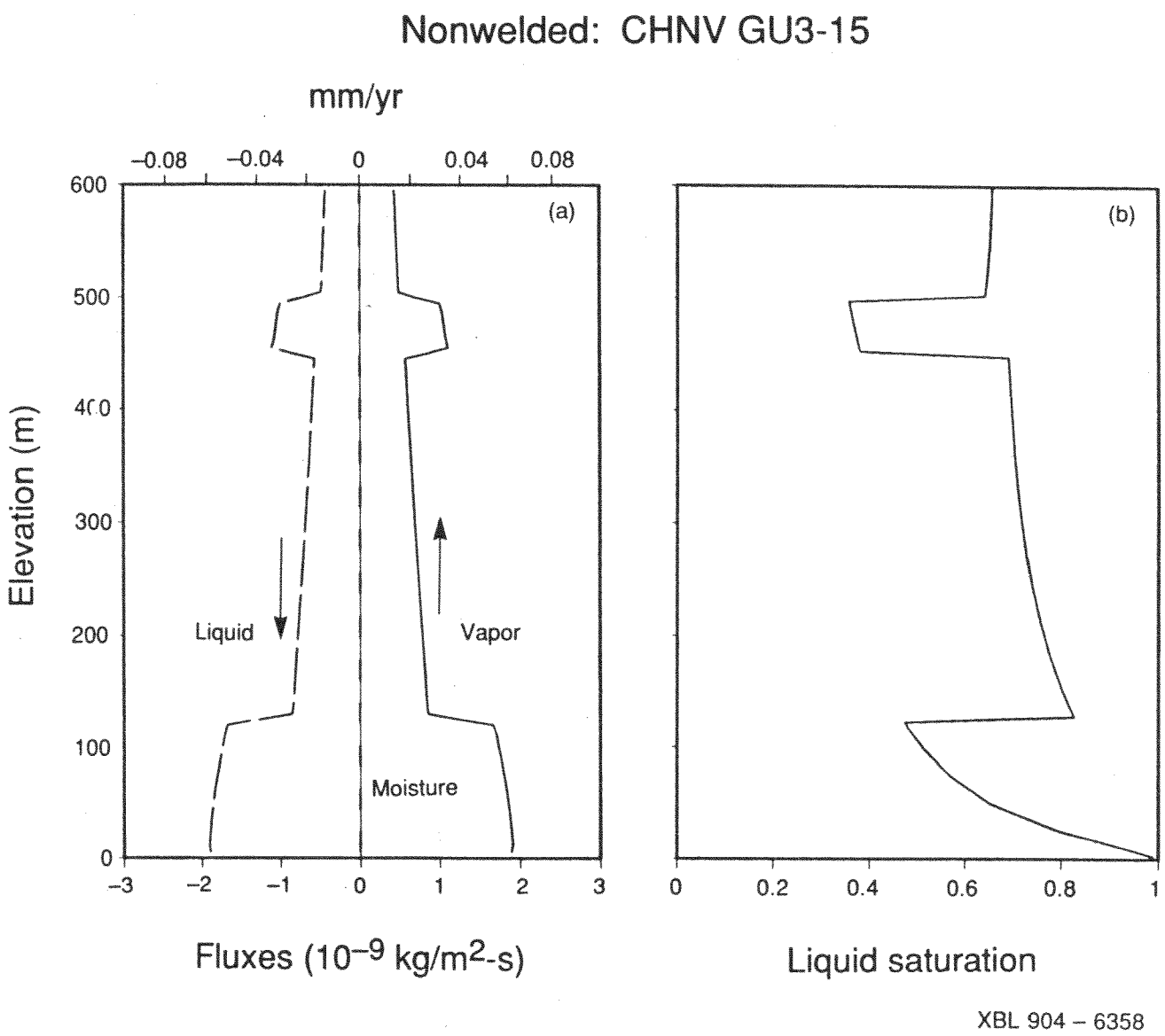

Figures 20. (a) Fluxes and (b) Liquid saturation profile for a layered column in the "reference case" (characteristic curves of Calico Hill sample #5 GU3-15 for the nonwelded units).

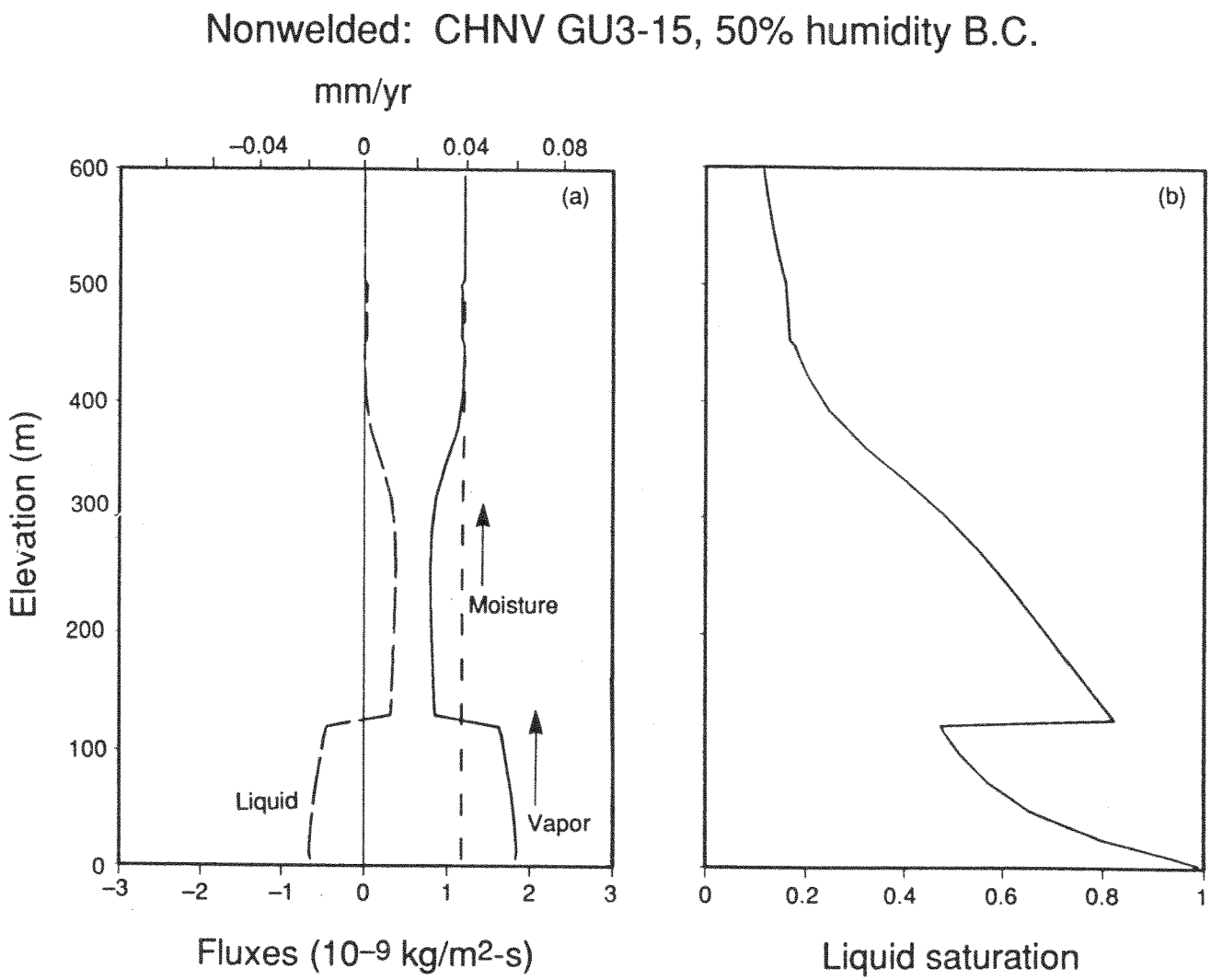

Figures 21. (a) Fluxes and (b) Liquid saturation profile for a layered column with 50% humidity boundary condition imposed (characteristic curves of Calico Hill sample #5 GU3-15 for the nonwelded units).

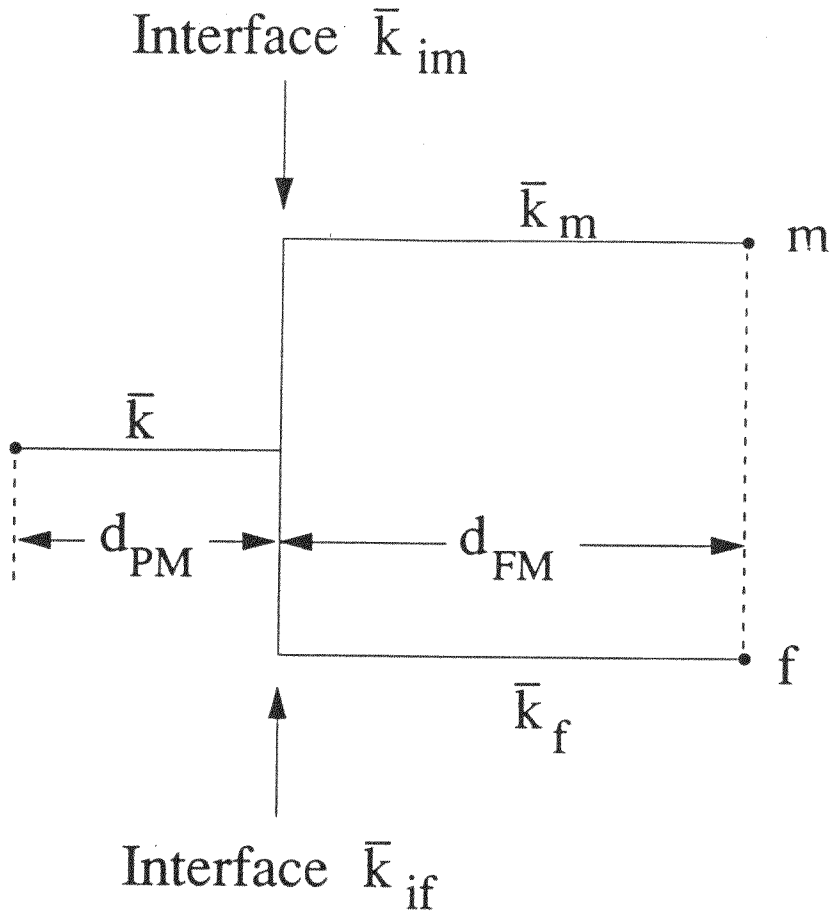

ESD-905-0005

Figure 22. Schematic diagram for explicit matrix and fracture description of the fractured medium at its interface with a porous medium.